317938
p. 140

AS&E®
American Science
and Engineering, Inc.
Fort Washington
Cambridge, Massachusetts 02139
617 868-1600
Telex 921-458 Fax 617 354-1054

29 NOVEMBER 1990

ASE-5752

SOLAR X-RAY ASTRONOMY ROCKET PROGRAM FINAL REPORT

NAS5-31619

PREPARED FOR:

NASA

GODDARD SPACE FLIGHT CENTER
WALLOPS FLIGHT FACILITY
WALLOPS ISLAND, VA 23337

ASE-5752

Final Report

Prepared for:

Contract No.:

Prepared by:

American Science and Engineering, Inc.
Fort Washington
Cambridge, Mass. [illegible]
617 [illegible]
Tel: 922-[illegible]
Fax: [illegible]

Date:

JEB-90-474

3 December 1990

Approved by:

Ms. Carol Taylor
Contracting Officer, Code 244.3
NASA/Goddard Space Flight Center
Wallops Flight Facility
Wallops Island, VA 23337

Subject: Contract NAS5-31619, Final Report

Dear Ms. Taylor:

In accordance with the provisions of Section C.2 of the subject Contract, American Science and Engineering, Inc. is pleased to submit one (1) copy of the Final Report for the Solar X-Ray Astronomy Rocket Program.

It has been a pleasure and a privilege to work with NASA on this project. It is rare to find such helpfulness and cooperation across the board from Technical as well as Contractual personnel.

Sincerely,

ASE

TABLE OF CONTENTS

LIST OF FIGURES

1. PROJECT SUMMARY

The goal of the AS&E Solar Physics Suborbital Program for NASA Contract NAS5-31619 is the study of the dynamics of the solar corona through the imaging of large scale coronal structures with AS&E High Resolution Soft X-ray Imaging Solar Sounding Rocket Payload. The proposal for this program outlined a plan of research based on the construction of a high sensitivity X-ray telescope from the optical and electronic components of the previous flight of this payload (36.038CS). Specifically, the X-ray sensitive CCD camera was to be placed in the prime focus of the grazing incidence X-ray mirror. The improved quantum efficiency of the CCD detector (over the film which had previously been used) allows quantitative measurements of temperature and emission measure in regions of low X-ray emission such as helmet streamers beyond 1.2 solar radii or coronal holes. Furthermore, the improved sensitivity of the CCD allows short exposures of bright objects to study unexplored temporal regimes of active region loop evolution.

Although the previous payload had been designed to permit straightforward reconfiguration to the anticipated needs of this program, several significant engineering efforts were obvious from the onset. The construction of the new payload involved the repair of the extensive structural damage sustained by 36.038CS upon recovery. Redesign of most of the damaged components was necessary to utilize, as much as possible, standard flight hardware from WFF. Design effort was also necessary to make provision for the acquisition of a photometric photographic image of the Sun to calibrate the CCD image with all the previous photographic images obtained with the three decades of solar physics at AS&E. The need for a photographic image with which to compare the CCD image became apparent in the analysis of the data obtained by 36.021CS and 36.038CS. Finally, the lack of repair support for the mid-seventies CCD image display computer (both for test and flight) as well as the obvious limitations in storage and processing capabilities of a computer of that vintage required the procurement of a new GSE computer and the associated system design.

The plans for the CCD payload were reconsidered when it became apparent that solar cycle 22 was unique in the rate and strength of its rising phase. The

need to review the hardware goals of this program were particularly strong in light of the lack of any organized space based effort to make comprehensive observations of the solar maximum until 1991. The scientific value of multi-spectral coordinated observations utilizing as a key component the X-ray photographic images from the AS&E rocket payload had been demonstrated in the X-ray Bright Point Observing Campaign of 1987 involving both 36.021CS and 36.038CS. At the Project Initiation Conference for this program in February of 1989 an option for a totally photographic payload was presented and listed in Appendix A of the Experiment Data Package in anticipation of this possibility.

The decision to pursue a photographic payload based on a coordinated observing campaign was made after the initial indication of a rapid rise to solar maximum was confirmed. A new AS&E Statement of Work for NAS5-31619 with the goal of participation in the Solar Active Region Observing Campaign was proposed in the 8 November 1989 letter to Dr. J. David Bohlin (AS&E ref. DM-89-L-205). This request was approved in the return letter of Dr. Bohlin dated 1 December 1989. The design studies previously initiated to provide both CCD and photographic images from a single flight demonstrated that the resources of the program would not support more than an all photographic mission. These designs are documented and will be useful to the further use of this payload in the NASA MSFC sounding rocket program. The new Statement of Work consisted of the following:

1) Refurbish the AS&E High Resolution Solar Soft X-ray Imaging Sounding Rocket Payload.

2) Provide a transfer of documentation, materials and data.

3) Support the Integration of the Payload at WSMR.

4) Continue data analysis efforts still underway.

5) Publish a Final Report.

The goal of the Solar Active Region Observing Campaign (SAROC), for which the AS&E payload was prepared, consists of obtaining high resolution observations of a large, complex sunspot group. From the data obtained during these operations, a new and unique data base that spans the full temperature range of the outer solar atmosphere, 4300 K through 10,000,000 K, will be assembled and used to investigate the physical processes that govern the dynamics of solar active regions and sunspots.

The observational resources for SAROC included two rocket borne instruments, the NRL High Resolution Telescope and Spectrograph (HRTS) and the AS&E X-ray telescope, both launched from White Sands, New Mexico and ground based observatories at Big Bear, California and at La Palma in the Canary Islands. Visible light instruments on the ground were to provide time series images of the photospheric magnetic fields and the intensity and velocity fields of the solar photosphere and chromosphere. The HRTS provided UV spectra that diagnose the densities, temperature and velocities of the temperature minimum region (4300 K), the chromosphere (10^4 K), the transition region (10^5 K) and flare-like plasmas (10^7 K). The AS&E X-ray telescope provided filtergrams to study the densities and temperature in the corona (10^6 K) and in flares (10^7 K).

One motivation for this program is the prominent theoretical explanation of the heating (or even the existence) of the corona based on the stochastic transport of the footpoints of magnetic loops by photospheric motions so that the resulting configuration is extremely complex and consequently capable of irreversibly dissipating any further work performed on the magnetic field configuration. It is expected that the observations obtained during SAROC will be used to gauge the success that such theories have in describing the heating and dynamics of the solar atmosphere in an active region and sunspot. Long term (10 hours) time series of the motions of the magnetic footpoints should provide a detailed estimate of the rate at which energy is fed into the system and the dissipation of this energy should be evident in coronal loops, microflares and explosive events observed by the rocket instruments. Other important phenomena such as the emergence of magnetic flux through the photosphere and its interaction with the pre-existing coronal field configuration can also be studied.

The SAROC was successfully conducted on 21 November 1990. The flights of 36.058CS and 36.060DS were launched at 11:15 and 11:40 MDT, respectively. The target region included one of the largest sunspot groups of this solar cycle. Significant magnetic shear was present in the vector magnetograms obtained by MSFC. The HRTS slit crossed a "tongue" of leader polarity which extended back into the trailer spot region. Two double ribbon flares were seen in the H-alpha images of the region, corresponding to the neutral lines associated with the "tongue" feature described above. Flares at the C2 and C3 X-ray level were in progress during each of the rocket flights. Clear skies and good winter seeing were present at BBSO while acceptable seeing was available at KPNO. The SOUP instrument was set up for observations at a location in Palo Alto, but the results of this effort is not clear at this time. All indications are that the observational programs of both rocket payloads were completely successful, but the film has not been processed from either payload. If the film developments are successful, the resulting data set will provide a unique perspective on solar activity in this cycle and prove more than well worth the effort.

2. DESIGN STUDIES

2.1. Prime Focus CCD and Film Camera Interchange Mechanism

A design study was made to investigate the feasibility of sequentially positioning the CCD Camera followed by the photographic camera at the prime focus of the grazing incidence X-ray mirror during a sounding rocket flight.

The proposed set up for this arrangement exclusively utilizes the following existing primary equipment: the 57 inch focal length grazing incidence X-ray mirror, the Multidata photographic camera, the X-ray sensitive CCD Camera, the flight sequencing on-board computer and the invar metered optical bench.

The photographic and the CCD cameras will be mounted so that they will be alternately placed in the prime focus of the X-ray mirror for exposures at various time intervals. Exposures could be made for a programmed sequence of time intervals while each camera is at the focus, or, using a reciprocating translation device, the two cameras could be alternately placed at the focus for each interval of a sequence of exposures.

The design of this experiment is based on the usage of a 17.26 inch diameter rocket payload with an internally usable diameter of approximately 15.00 inches. The design is also subject to the constraints of (1) the geometric shape and sizes of the two cameras used, (2) the amount of translation and aspect of the translation to the prime focus, (3) the load capacity of translation and drive mechanism and (4) the resolution of translation drive to achieve precisely the prime focus position. Due to these constraints, the photographic camera mount and the CCD camera dewar housing will also have to be slightly modified in this new design.

Figure 1 shows the layout drawing developed to verify the concept. Mechanical arrangement of this package is such that the photographic camera and the CCD Camera are both mounted on the same cradle. This cradle rides on a pair of precision linear bearing guide rails and blocks to assure a smooth and repeatable linear motion.

FOLDOUT FRAME

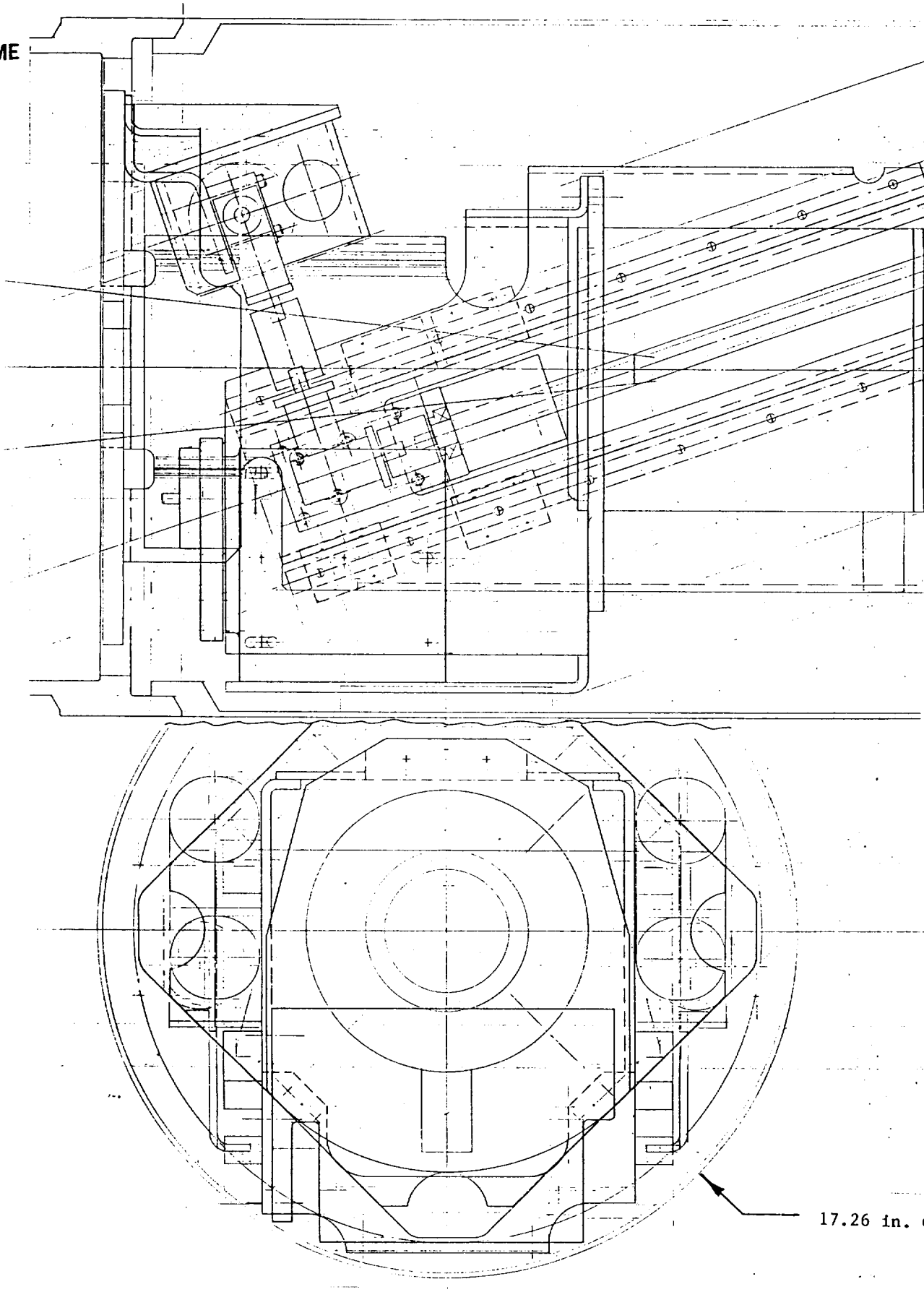

Figure 1: Developmental layout drawing prepared to verify the feasibility of the photographic and CCD camera interchange mechanism.

2.

FOLDOUT FRAME

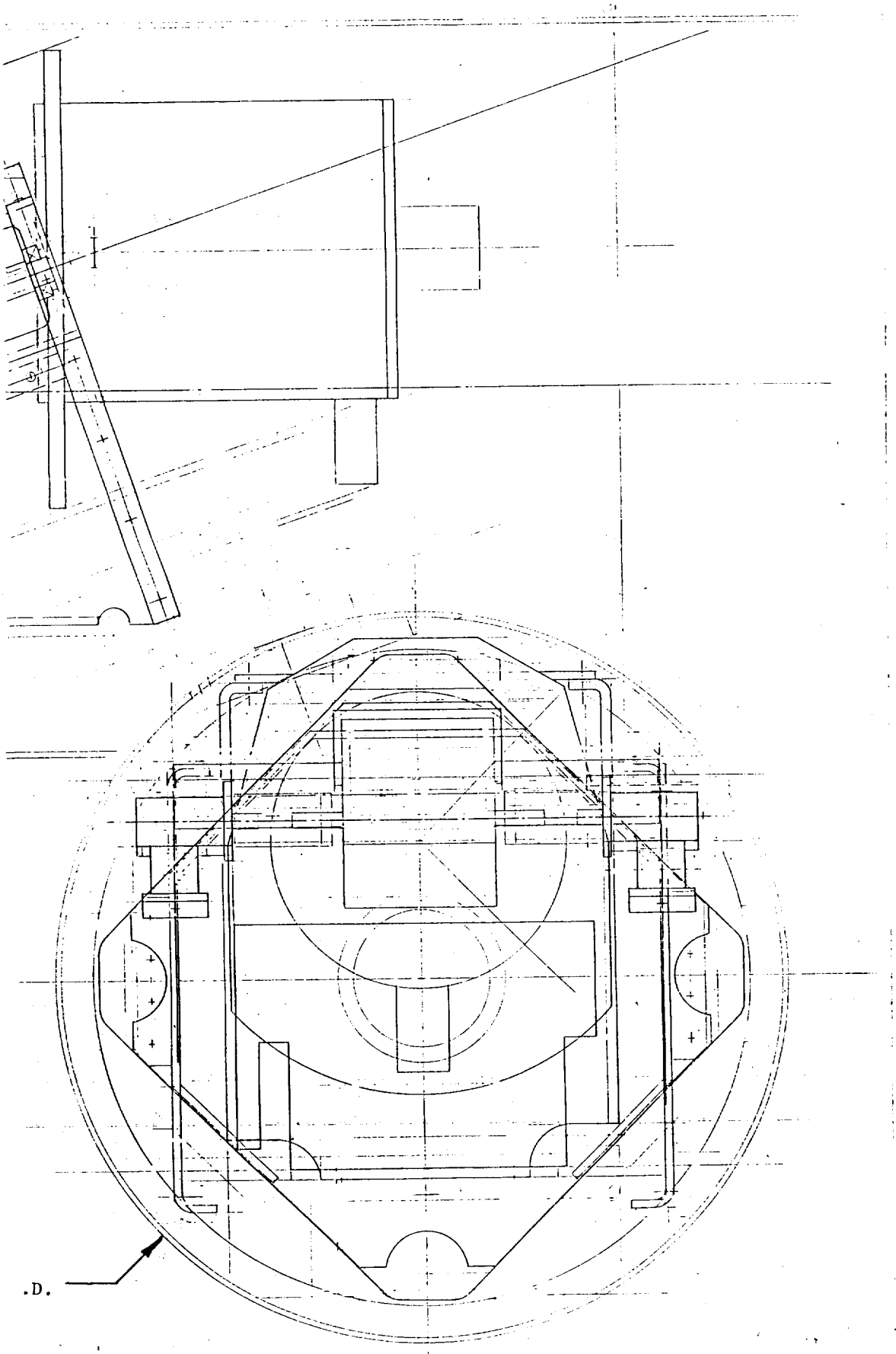

.D.

The camera cradle is designed to travel on the translation stages at an angle of 19 degrees to the payload thrust axis. The proposed translation mechanism will employ a pair of planetary roller screws, one at each side of the camera cradle, driven by permanent magnet direct current motors. The extra clearance required for the photographic camera when the CCD camera is in the imaging position is obtained by shortening the optical bench by approximately 6 inches and maintaining the focal position with the structure of the new assembly. This is easily accomplished with the current optical bench design.

Operating redundancy is a requirement of the system design. To fulfill this requirement, a differential gear box is used, driven by two independently powered DC planetary gear motors to assure redundancy in the drive for the translation system.

Figure 2 provides a tabulation of all components (together with vendors) critical to the implementation of the design. Miscellaneous drive components and couplings are also needed in conjunction with the key components to complete the drive system. The complete translation system will be housed in a support structure mounted to the same bulkhead to which the optical bench is mounted.

The preliminary effort put to the study of this arrangement clearly showed that a functional camera change mechanism could be incorporated into the payload. All existing available flight cameras and optics would be used. Some new mechanical support structure, a drive system and miscellaneous hardware items would have to be developed or procured. The mounting bulkhead for this new arrangement is the existing hardware item, but the payload skin will have to be redesigned to accommodate the new payload assembly.

Item	Description	Part No.	Manufacturer
1	Right Angle Gear Drive	RA 621, Ratio 1:1	Boston
2	Linear Motion Guide	HSR 15TR 244-460L	THK
3	DC Planetary Gear Motor	TBD	TRW Globe
4	Planetary Roller Screw	TBD	Spiracon
4 alternate:	Rollnut	TBD	Norco
5	Differential Drive Assembly	16 pitch miter gears, .375 in. shafting and 3000 in-oz torque cap.	Allied Devices or FAE Industries

Figure 2: Tabulation of critical parts required to implement the sliding camera interchange mechanism.

2.2. Nested Photographic Imager Using a Six Inch Diameter Grazing Incidence Telescope

Another study was performed to investigate the feasibility of adding a second X-ray telescope and photographic camera to the current payload as an alternative to the camera interchange mechanism described in the previous section. A secondary motivation behind the study was to add a 33 inch focal length X-ray mirror available to the sounding rocket program from an earlier NASA project and evaluate its performance in comparison to the current mirror in an upcoming flight. This X-ray telescope is a nickel coated beryllium mirror, 5.5 inches in aperture diameter, and fabricated under AS&E's International Solar Polar Mission (ISPM) Coronal X-ray imager project. A flight qualified Cannon 35 mm automatic photographic camera was obtained on loan from Prof. A. B. C. Walker of Stanford University for use in this study.

The design constraints to add the second camera systems are the same as described above under the other study. The current primary mirror (57 inch focal length) and primary camera (photographic or CCD) will stay in their established locations. The secondary mirror (33 inch focal length) will be mounted on a piggy-pack type arrangement and nested in the center bore area of

the primary mirror. The exact positioning of the secondary mirror will be determined by the location and size of the secondary camera which will have to be positioned to lie fully within and clear of the innermost optical ray paths of the primary grazing incidence mirror.

This requirement can be achieved by positioning the Cannon camera at a minimum distance of 41 inches from the primary focal plane, allowing an 8 inch diameter clearance circle perpendicular to the optical axis. The secondary mirror would then extend about 16 inches in front of the primary mirror. In this arrangement, the forward and aft aperture plates of the primary mirror will have to be modified to accommodate the nesting installation and X-ray passage of the secondary mirror.

2.3. Ground Support Computer for CCD Image Display

Because of the aging of the current Ground Support Equipment (GSE) computer for software development and maintenance of the CCD camera system a survey was made and a cost estimate was prepared to replace the computer with a commercially available desk top computer system. The survey resulted in the selection of a MacIntosh IIx computer and application software as described in Appendix A.

Similarly, because of the aging of the current data analysis and image display station, based on a Data General NOVA 4 computer and a Lexidata display controller, a survey was made and a cost estimate was prepared to replace this equipment with a commercially available imaging workstation. The survey resulted in the selection of a Sun Microsystems SPARCstation 1 system and application software as describe in Appendix B.

3. PAYLOAD REFURBISHMENT

3.1. Repair of Damage Sustained in Flight 36.038CS

The payload of flight 36.038CS, descending by parachute, landed on the side of a steep slope and consequently rolled down the incline a substantial distance before coming to rest. This hard landing caused very extensive damage to the extension of the payload. The external skins including the aperture door and mechanism were damaged beyond repair. Damage was severe enough that in order to remove the optical bench and telescope, the skins had to be cut away. On removing the interval components, it was found that the optical bench, X-ray telescope mirror, electronics rack and other interval components all survived intact. Therefore, only the external components required rebuilding. For reasons of both cost and future adaptability and maintainability of the payload, a decision was made to acquire a standard aperture door and mechanism from Wallops Flight Facility and modify the designs of the replaceable impact crush section, optical bench mounting bulkhead and payload skins as descended below.

3.1.1. Telescope Aperture Door and Crush Section

The Wallops developed aperture door has been flown by other investigators on numerous flights and has proven reliable. It was available immediately for WFF and its performance meets or exceeds the requirements of the payload experiment. Since new skins were being designed the new mechanical interface was easily accommodated. Because the subsystem has already been flight qualified, payload testing with the new design was much simplified.

The impact protection (Crush) section requires rebuilding after each flight. However, the section was also redesigned to be compatible with the new aperture door subsystem. The aim of the redesign included simplification of fabrication while retaining the same impact absorbing characteristics. A section of this new design was fabricated in AS&E'S Machine Shop the refurbished payload and a substantial savings in the fabrication hours resulted.

3.1.2. Optical Bench Bulkhead

The Optical Bench Bulkhead, which interfaces the X-ray telescope with the payload structure and skins was similarly redesigned to economize in assembly time and adaptability to future modification. The new design facilitates telescope to payload alignment while employing shorter skin sections. The bulkhead was also made to interface directly to the payload dolly without the skins in place for much greater ease in handling and in payload integration and check out. The routing through and around the bulkhead of system cables was also greatly simplified over the old design.

3.1.3. Payload Skins

The old payload skin design was not well suited for the photographic camera and CCD camera instruments. The design was inadequate in overall length and in access ports for instrument servicing. Therefore, new skins were designed which are modular in configuration with the basic module well suited for the current photographic camera instrument and for a combined photographic and CCD camera instrument. Other skin modules may be added if more experiments are to be included in a given flight. Service access requirements were reviewed for use both in the laboratory or at the launch facility. The new access requirements were incorporated into the designs for the new skins, overcoming the earlier shortcoming. New skins were fabricated and integrated with the refurbished payload.

3.2. Prefilter Mount Redesign

The existing prefilter mount had been fabricated from this (.032 inch) aluminum with minimal stiffening members. Over the course of several flights and refurbishments, the mount has become distorted. As a result an attempt to mount a new prefilter resulted in wrinkling and rejection of the mounted pre-element. A new mount was therefore designed and fabricated. The new mount was machined from a single piece of bar stock aluminum. Integral stiffening ribs were machined entirely around the filter element mounting areas. This design

eliminated the distortion potential of the old design while its shape and mounting bolt pattern replicated that of the old Design.

3.3. Photographic Camera Refurbishment and Characterization

Sometimes questionable performance of the aging, 20 year old Multidata photographic cameras, around which the X-ray imaging payload is designed, resulted in a complete characterization and overhaul of the cameras. The details of the characterization are provided in Appendix C. Overhaul of the cameras was subcontracted to Flight Research Corporation.

3.4. H-alpha Aspect Camera Filter Refurbishment

The poor performance of the H-alpha aspect camera system during 36.021CS and 36.038CS was traced to also aging, in this case of the H-alpha filter in the system. The filter was returned to Day Star Co. for refurbishment. Shock damage from previous flights was found to have caused the destruction of both the etalon and blocking filter. Therefore, a completely new filter was fabricated and installed in the existing filter mount. The resulting aspect system demonstrated superior performance in the sun tracking phase of the integration tests at White Sands Missile Range.

3.5. X-ray Filter and Pre-filter Procurement

Prefilters and the thinnest of the X-ray filters are too fragile to survive recovery and therefore are replaced after every flight. The prefilters have always been procured from Luxel Corp., Friday Harbor, WA. An unsupported, free-standing aluminum filter of thickness of 2000 angstroms was again procured from Luxel. With the prefilter mount redesigned as described in Section 3.2, above, this process was simplified. However, vibration survivability tests on these filters in the new mounts cast doubt on their suitability for use in flight. The new design of the filter mount is suspected to improperly isolate the filter from the vibration environment.

Aluminized polypropylene filters are also required for the long wavelength images. The fabrication of 1 micron thick polypropylene filter membranes is done at AS&E. However, the capacity to provide a pinhole-free aluminum coating is a process which must be subcontracted. Excellent coatings were obtained from Acton Research Corp. (ARC), Acton, MA, in 1987. However, ARC was unable to provide successful coatings for an order under the current program. The loss of capability was unexplained. A successful attempt a coating the membranes was made by Luxel following the ARC failure. Although a few iterations were required to perfect their technique, the final coated membrane filters were excellent. The cooperation and assistance of Luxel to meet a critical need in this and in other extenuating situations is to be highly commended.

3.6. Cleaning of the Twelve Inch X-ray Grazing Incidence Telescope

The 12" fused quartz main mirror was cleaned in a four step process to remove dust and hydrocarbon contaminants. Care was taken to avoid any undue pressure which might cause any particulates to scratch the mirror surface. The washing process can be described as one washing step and three rinsing steps. The first step consisted of soaking the mirror assembly in a three percent solution of Liquinox brand laboratory glassware liquid soap in distilled water. The mirror was completely immersed and allowed to soak for two to three hours. This would allow the soap to gently work the dust and hydrocarbon contaminants free from the mirror's surface. This soaking period was followed by a swabbing of the surface with loose sections of sterilized, combed cotton batting. The cotton was rotated as it swabbed the surface to lift the contaminants from the mirror's surface. The cotton batting was rotated through only one revolution so as not to allow the removed contaminants to come in contact with the mirror again. The cotton was then discarded. After this swabbing procedure was completed, the mirror was removed from the bath and rinsed completely with distilled water. Approximately thirty gallons of distilled water were used for this step and all parts of the mirror assembly were rinsed. The second rinse was designed to remove water from the mirror assembly and to further remove any persistent hydrocarbon contamination. The rinsing agent chosen was pure ethyl alcohol. This type of alcohol absorbs water and when drying, leaves little or

no residue. The third rinse was designed to remove any residue from the second rinse that may have been left. The rinsing agent chosen was anhydrous ether. Ether leaves no residue after it evaporates, while the flow combined with solvent properties of ether will remove any hydrocarbon films remaining on the mirror's surface. The mirror was then covered to prevent any dust from accumulating until performance measurements were required.

4. CALIBRATION

4.1. Filter Assembly Refurbishment and Calibration

4.1.1. General

The filter wheel has five different filter positions. These positions contain the following:

1. A 1.0 mil Beryllium filter.
2. A 0.5 mil Beryllium filter.
3. A 1 micron polypropylene filter with a coating of 2000 angstroms of aluminum for white light rejection.
4. A free standing 1500 angstrom aluminum filter.
5. A white light filter pack consisting of neutral density filters with a value of 5.3 and a Kodak #99 green filter.

All filters with the exception of the white light filter pack were mounted on an aluminum filter ring with a clear aperture of 1.15 inches. The filter rings have three holes equally spaced and tapped to accept 0-80 screws. The white light filter pack was sandwiched between the filter ring and the filter wheel. The filter wheel is housed inside the 35 mm film camera. The filter wheel position is monitored by a microswitch on the front of the camera activated by a cam on a shaft driven directly by the filter wheel. This cam only indicates the position of position number 1, the rest of the positions are determined by the computer keeping track of the filter advances.

4.1.2. Beryllium Filters

The beryllium filters were made by selecting a region of a stock sheet that contained no pinholes. The filter was then mounted to the filter ring by Devcon 5 minute Epoxy.

4.1.3. Aluminized-Polypropylene Filters

The aluminized polypropylene filters were made by AS&E and Luxel Corp., as Described in Section 3.5, above. The thickness of the polypropylene substrates

were measured using the transmission of Carbon K-alpha X-rays (0.275 keV) through the substrate and comparing it to the direct X-rays from the source. The source of X-rays was a ^{244}Cm alpha particle emitter bombarding a graphite target to give the 0.275 keV X-rays. A measurement of the characteristic background radiation was included to improve accuracy. Using the known attenuation of polypropylene at this X-ray energy (-1755.7 per cm), the thickness was then calculated. Acceptable values for the thickness of the polypropylene substrate range from 0.95 to 1.1 microns. Measurements of the polypropylene disks are tabulated in Figure 3, below.

	Average Measured Counts:			Calculated
Disk No.	Source	Attenuation	Background	Thickness
66	50944	61141	458	1.050×10^{-4} cm
67	53726	64405	458	1.039×10^{-4} cm
68	53567	64866	458	1.098×10^{-4} cm
69	73326	61538	468	1.005×10^{-4} cm
70	73951	62746	468	0.942×10^{-4} cm

Figure 3: Tabulation of measured X-ray counts and calculated thicknesses for the substrates of the Aluminized-Polypropylene filters.

4.1.4. White Light Filter

The white light filter was composed of Kodak neutral density filters with a value totaling 5.3 and a Kodak Wratten #99 green filter. These filters were cut to shape and held in place with a filter frame.

4.2. Photographic Film Sensitometric Calibration

Calibration of the flight film was obtained with the inclusion of a series of X-ray step wedges during the flight film processing. These sensistrips were made on film from the same roll as the flight load and were exposed to a

predetermined photographic density. The sensistrips were used to obtain a relation of the photographic density of a film X-ray exposure to the amount of energy deposited and to monitor the film processing. The sensistrips were exposed to aluminum K-alpha line X-rays in sensitometers made with twenty four steps of aluminum foil. Each step has a transmission to aluminum X-rays (1.5 keV) of T = 0.5118. The required exposure for the densest step is typically 227 erg/cm^2. To reach this desired energy density, 9.486 X 10^{10} photons from an aluminum K-alpha X-ray source were required to reach the film. In order to monitor this exposure, a flowing gas proportional counter was placed at a position where it would receive an equivalent dose. The window of the counter consisted of:

1) a beryllium window, T = 0.4483 to aluminum X-rays
2) low pressure detector gas with an efficiency of 0.9761
3) 8 layers of thin Al foil, T = (0.5118) X ^{8}
4) a 1000 micron pinhole, Area = 7.854 X 10^{-3} cm^2.

Combined, these give an efficiency of 1.537 X 10^{-5}. The number of photons required to be detected in the counter at this efficiency then becomes 1,492,148 and the exposure time is approximately an hour with a count rate of 500 counts/sec. Sensistrips are made shortly before the film development with several being used on each process. There are typically two strips attached to both the leader and trailer of the flight film strip. Other sensistrips are used to calibrate different film processors and chemical processes prior to developing the flight film. The processor and process parameters are then selected to achieve the optimum exposure latitude (dynamic range) in the flight film images.

4.3. Grazing Incidence Telescopes Calibration

The total collecting area of the rocket primary mirror and the International Solar Polar Mission (ISPM) mirror were measured. The measurements were made using the Long Tube Facility (LTF) at AS&E. The LTF uses a fine focus X-ray source that can be made to give pure X-ray spectral lines by the bombardment of pure element anodes by electrons. The focal spot can be either of two sizes, 100 micrometers x 100 micrometers or 1000 micrometers x 100 micrometers, depending on whether high flux or a well defined point source is required. The

distance from the focal spot to the optical components is 91.8 meters. The LTF can sustain a vacuum of better than 4×10^{-6} torr.

The sounding rocket mirror throughput was measured at the 44.54 Angstrom Carbon K-alpha line for the sounding rocket mirror. The ISPM mirror throughput was measured at both the 8.32 Angstrom aluminum K-alpha line and the 44.54 Angstrom Carbon K-alpha line since it has significant response at the shorter wavelengths. The X-ray source accelerating potential was run at two times the photon energy at the selected wavelength (i.e., the accelerating potential used to generate aluminum K-alpha lines at 8.3 angstroms and 1.5 keV photon energy is 3 kV). Spectroscopic tests have shown in the past that the spectral line purity is very good at such acceleration potentials while the flux is high.

The optical bench on which the optics were placed was capable of being pivoted about the telescope entrance aperture over a range of 3 degrees with orientation known to 2 arcseconds. Each mirror was first autocollimated into rough alignment with the X-ray source. A proportional counter monitor with a known aperture was positioned for each test at the front surface of the mirror so as to receive the same flux. Another counter is positioned at the mirror focus. The two counters were previously cross-calibrated and found to have a 6% difference in counting response.

Figure 4 shows a plot of the measured effective collecting areas (throuhputs) of the mirrors at the selected wavelengths as functions of the angle between the mirror axis and the line of sight to the X-ray source. The measured points are shown and a line is sketched roughly through the points of each data set to more clearly show the groupings of the data sets. AS&E's X-ray ray trace program was also used to calculate the effective collecting areas versus angle of incidence. The three smooth curves are the calculated collecting areas as indicated, reduced by 10 percent for aperture support obscurations. It should be noted that for the measured data sets, the zero value of angle of incidence is taken to be at the maximum throughput measured for that mirror. This is somewhat arbitrary and could result in the shifting of the measured curves to the left or the right. For the two measurements at different wavelengths on

the ISPM mirror, the two data sets are assumed to have the same zero offset in the angles of incidence. Thus the data at the aluminum K_alpha line has no points in the vicinity of 0 arcminutes on the graph in accordance with the way the data was taken.

Figure 5 shows full spectral plots of effective collecting area as calculated by the raytrace program at 0 arcminutes angle of incidence, again reduced by 10 percent for aperture obscurations, for the two mirrors. The maximum of the measured points at each wavelength for the two mirrors is shown on the plots for comparison. The roughly 30 percent lower measured values below those computed by the program could relate to particulate contamination of the mirrors, but is generally not Understood.

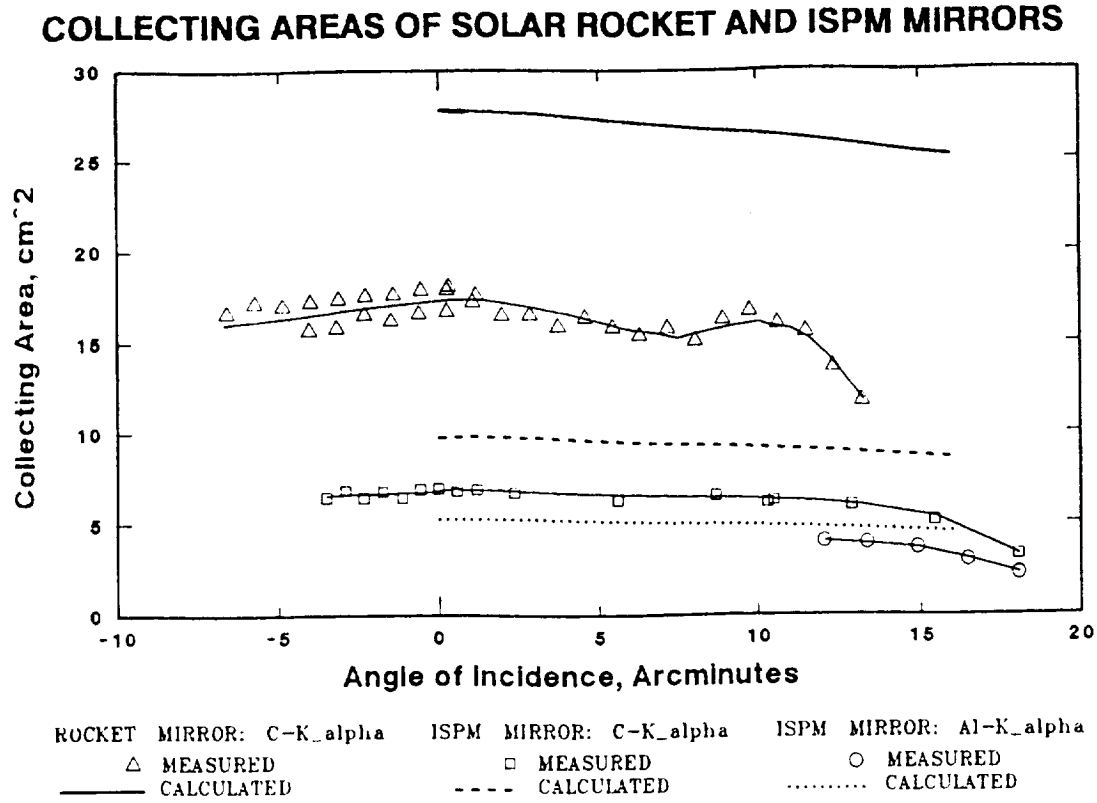

Figure 4: Effective collecting areas (measured and calculated) versus line of sight angle for the sounding rocket and ISPM telescope mirrors.

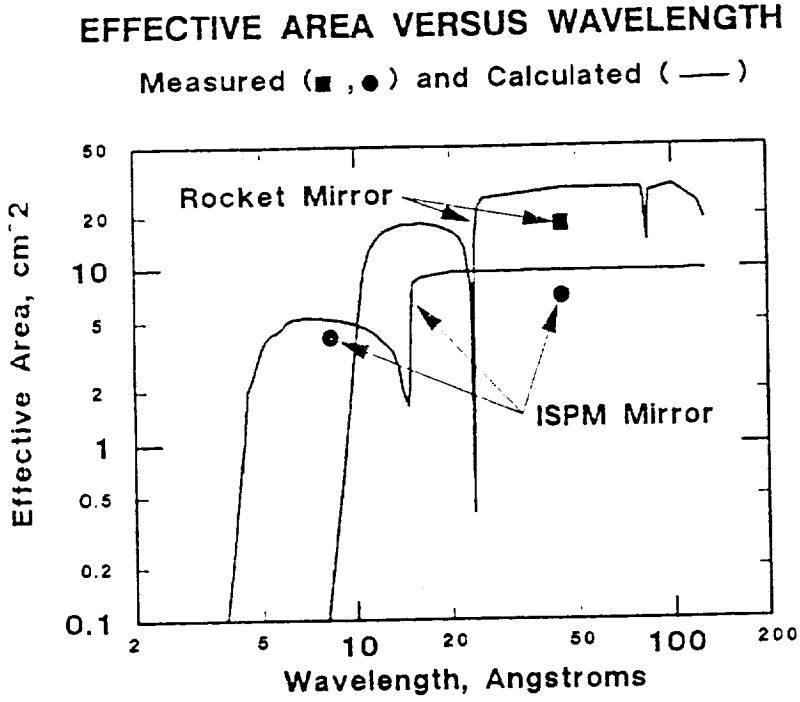

Figure 5: On-axis effective collecting areas (measured and calculated) versus X-ray wavelength for the sounding rocket and ISPM telescope mirrors.

5. INTEGRATION SUPPORT

Following the refurbishment of the payload, it was readied for shipment to White Sands Missile Range (WSMR) in anticipation of a June 1990 launch. The payload and support equipment was then first shipped to the Naval Research Laboratory in Washington, DC, where it was transhipped, together with an NRL sounding rocket payload, to WSMR.

On arrival at WSMR, the payload was unpacked and checked out. For the final integration and optical alignment of the payload with the sounding rocket booster and other subsystems, AS&E provided on site support at WSMR. AS&E thereafter continued to support the readiness of the payload for flight with X-ray sensitometric calibrations of film and technical consultations by phone.

6. CONTINUED ANALYSIS OF DATA FROM 36.021CS AND 36.038CS

The analysis under the current contract of data from the two previous flights has resulted in the preparation of a journal paper for imminent publication. Appendix D contains a preprint of this papers. A second paper is in preparation by D. F. Webb (AFGL), et. al.

7. FOLLOW-ON CONTINUITY

The continuance of solar rocket research in the soft X-ray regime will be under a new principal investigator Dr. J. M. Davis and institution, NASA/Marshall Space Flight Center. In order to retain the greatest benefit to on-going research from earlier programs, NASA/HQ (Dr. D. Bohlin) directed the transfer of all government property accountable to the current program as well as data products accumulated under prior solar research at AS&E, to the new PI and institution. The data products included those from the solar rocket research programs and the Skylab/Apollo Telescope Mount S-054 experiment. Digitized image data from the S-054 experiment that was stored on computer magnetic tape were directed by NASA/HQ to go to the National Space Science Data Center in

Maryland. These transfers were coordinated under and completed during the closing months of the program.

The transfer of digitized S-054 soft X-ray images of the sun was made to Dr. David Batchelor, Solar Acquisitions Scientist, NASA/Goddard Space Flight Center. Over 560 tapes (IBM format, 2400 feet) were delivered.

The new PI reviewed lists of equipment to be transferred and accepted most of the items and directing that certain of the older and less useful items be declared surplus to the government. Through this process all government property accountable to the current contract has been transferred to NASA/MSFC or is being processed as surplus by DCMAO-Boston-FAMN.

Significant data products transferred to NASA/MSFC include all original exposed and processed photographic negatives from both S-054 and the solar rocket research programs as well as several sets of enlargement internegatives made from the original negatives suitable for use in future research efforts. Other, ancillary records were also transferred, including computer analysis programs, in an effort to keep together as much of the body of knowledge accumulated in the programs as possible.

Documentation in the form of drawings covering the current rocket payload configuration as well as earlier payload configurations were also transferred to NASA/MSFC. These drawings include the documentation of the CCD and GIRO camera elements used in the 36.021CS and 36.038CS flights. Appendix E contains a list prepared of the mechanical drawings.

APPENDIX A: ESTIMATE FOR REPLACEMENT OF THE GSE (BLUE) COMPUTER WITH A MACINTOSH IIx COMPUTER

Estimate for replacement of the Blue Computer

with a Macintosh IIx computer

Prepared by: M. A. Purinton

Date: June 27, 1989

Summary

Option #1 ; TrueVision, Inc. Image Processor

1. Computer and related hardware	$ 20330
2. Purchased Software	$ 2190
3. Hardware Development	72 M.M.
4. Software Development	292 M.M.

Summary

Option #2 ; Automatix, Inc. Image Analyst, MacRail and MacRail's "C" Libraries with the low priced monitor

1. Computer and related hardware	$ 19360
2. Purchased Software	$ 11390
3. Hardware Development	72 M.H.
4. Software Development	214 M.H.

Summary

Option #3 ; Automatix, Inc. Image Analyst, MacRail and MacRail's "C" Libraries with the E-Machines gray scale display monitor

1. Computer and related hardware	$ 20305
2. Purchased Software	$ 11390
3. Hardware Development	72 M.H.
4. Software Development	214 M.H.

June 23 , 1983

ppared by: M. A. Purinton
vision 0.00.00

tion no. 1 TrueVision, Inc. Image Processor Display

H A R D W A R E

ple MAC IIx computer with 5 MB of dram, 3 1/2" 800 Kbytes floppy disk drive
321 Mbytes (formatted) internal hard drive, extended keyboard.
- includes SCSI bus interface and cables for disk drives
- includes Apple mouse and Multi-Finder OS
- includes Model 1302 Color / B&W RGB monitor with 256 gray levels
- does not include video controller card (see below) $10110

ueVision Inc. Image processor video card $ 3370
- NuVista 1M
- Color and B&W modes
- RGB output with sync signal
- compatible with Apple's 32 bit Quick-Draw interface
- 1024x1024 16 bit addressable resolution

ueVision Inc. Image processor video card to monitor cables $ 50

ple Imagewriter II dot matrix printer $ 1000

ple Imagewriter II dot matrix printer cable $ 30

rc Systems NuSuper RISC Coprocessor $ 4000
- includes 2 MB of high speed RAM for instruction memory
- includes 1 MB of DRAM for data storage
- 50 Mhz clock rate

nsington Turbo Mouse (Trackball) ADB #62360 $ 170
- includes cable
- includes second ADB port
- additional button over mouse

erson Computer Power PC-ET A.C. line conditioner $ 800
- 3 A.C. power outlets
- 360-VA output
- noise filtering and spike suppression

rallel Interface for Telemetry Input $ 800

Sub-total $ 20330

epared by: M. A. Purinton
vision 0.00.00

June 23 , 1983

tion no. 2 Automatix's Image Analyst, MacRail and MacRail's C Libraries with a low priced display monitor

H A R D W A R E

ble MAC IIx computer with 5 MB of dram, 3 1/2" 800 Kbytes floppy disk drive 321 Mbytes (formatted) internal hard drive, extended keyboard. - includes SCSI bus interface and cables for disk drives - includes Apple mouse and Multi-Finder OS *- includes Model 1302 Color / BW RGB monitor with 256 gray levels - does not include video controller card (see below)	$10110
gnovox 14" 640x480 BW Display Monitor - ADB - includes fine dot pitch - tilt & swivel base	$ 300
bit video controller card and cable	$ 650
MB of dram memory board upgrade	$ 1500
ple Imagewriter II dot matrix printer	$ 1000
ple Imagewriter II dot matrix printer cable	$ 30
rc Systems NuSuper RISC Coprocessor - includes 2 MB of high speed RAM for instruction memory - includes 1 MB of DRAM for data storage - 50 Mhz clock rate	$ 4000
nsington Turbo Mouse (Trackball) ADB #62360 - includes cable - includes second ADB port - additional button over mouse	$ 170
ferson Computer Power PC-ET A.C. line conditioner - 3 A.C. power outlets - 360-VA output - noise filtering and spike suppression	$ 800
rallel Interface for Telemetry Input	$ 800
Sub-total	$ 19360

epared by: M. A. Purinton
vision 0.00.00

June 23 , 1983

tion no. 3 Automatix's Image Analyst, MacRail and MacRail's C Libraries with the E-Machines gray scale display system

H A R D W A R E

ple MAC IIx computer with 5 MB of dram, 3 1/2" 800 Kbytes floppy disk drive 321 Mbytes (formatted) internal hard drive, extended keyboard. - includes SCSI bus interface and cables for disk drives - includes Apple mouse and Multi-Finder OS *- includes Model 1302 Color / B&w RGB monitor with 256 gray levels - does not include video controller card (see below)	$10110
E-Machines Model #1008-IQ Display Monitor - ADD - includes video controller and cables - 17" 60hz monitor with 256 gray levels - 1024x808 pixel format	$ 1895
MB of dram memory board upgrade	$ 1500
ple Imagewriter II dot matrix printer	$ 1000
ple Imagewriter II dot matrix printer cable	$ 30
irc Systems NuSuper RISC Coprocessor - includes 2 MB of high speed RAM for instruction memory - includes 1 MB of DRAM for data storage - 50 Mhz clock rate	$ 4000
nsington Turbo Mouse (Trackball) ADB #62360 - includes cable - includes second ADB port - additional button over mouse	$ 170
erson Computer Power PC-ET A.C. line conditioner - 3 A.C. power outlets - 360-VA output - noise filtering and spike suppression	$ 800
rallel Interface for Telemetry Input	$ 800
Sub-total	$ 20305

epared by: M. A. Purinton
vision 0.00.00

June 23 , 1983

tion no. 1 TrueVision, Inc. Image Processor Display

S O F T W A R E

rtran 77 (VAX compatible extensions) - includes Apple's MPW development environment - interfaces to assembly and C programs compatible with the MPW environment	$ 500
ghtspeed C Compiler for the MAC II in conjunction with the Truevision Inc. image processing board.	$ 200
ueVision, Inc. image processor Microsoft C library routines (Source code)	$ 50
rc Systems NuSuper S/W - Macintosh II Linker and Debugger	$ 200
rc Systems NuSuper N"C" - Metraware Native "C" compiler for the 29K processor and runs on the AMD29000 coprocessor board	$ 900
7/8" x 11" 1/2" green bar paper (Qty: 3 boxes)	$ 100
ple Imagewriter II printer ribbons (Qty: 12 ribbons)	$ 40
1/2" 800K floppy disks (Qty: 200 floppies)	$ 200
Sub-total	$ 2190

epared by: M. A. Purinton
vision 0.00.00

June 23 , 1983

tion no. 2 Automatix's Image Analyst, MacRail and MacRail's C Libraries with a low priced B&W monitor.

S O F T W A R E

ortran 77 (VAX compatible extensions) - includes Apple's MPW development environment - interfaces to assembly and C programs compatible with the MPW environment	$ 500
pple C Compiler for the MAC II in conjunction with the Automatix, Inc. image display software.	$ 200
utomatix, Inc. Image Analyst Program Product No. AM3000 (MacRail Source and runtime code)	$ 2000
utomatix, Inc. MacRail Program (Runtime and development code)	$ 4500
utomatix, Inc. MacRail C libraries Product No. AM3110 (source, object and link procedures)	$ 2000
utomatix, Inc. Image Analyst and MacRail Upgrade Service (twice a year update) Product No. AM3500	$ 750
rc Systems NuSuper S/W - Macintosh II Linker and Debugger	$ 200
rc Systems NuSuper N"C" - Metrowerks Native "C" compiler for the 29K processor and runs on the AMD29000 coprocessor board	$ 900
7/8" x 11" 1/2" green bar paper (Qty: 3 boxes)	$ 100
pple Imagewriter II printer ribbons (Qty: 12 ribbons)	$ 40
1/2" 800k floppy disks (Qty: 200 floppies)	$ 200
Sub-total	$ 11390

epared by: M. A. Purinton
vision 0.00.00

June 23 , 1983

tion no. 3 ---------- Automatix's Image Analyst, MacRail and MacRail's C Libraries with an E-Machines gray scale display monitor.

S O F T W A R E

rtran 77 (VAX compatible extensions) - includes Apple's MPW development environment - interfaces to assembly and C programs compatible with the MPW environment	$ 500
ple C Compiler for the MAC II in conjunction with the Automatix, Inc. image display software.	$ 200
tomatix, Inc. Image Analyst Program Product No. AM3000 (MacRail Source and runtime code)	$ 2000
tomatix, Inc. MacRail Program (Runtime and development code)	$ 4500
tomatix, Inc. MacRail C libraries Product No. AM3110 (source, object and link procedures)	$ 2000
tomatix, Inc. Image Analyst and MacRail Upgrade Service (twice a year update) Produt No. AM3500	$ 750
rc Systems NuSuper S/w - Macintosh II Linker and Debugger	$ 200
rc Systems NuSuper N"C" - Metreware Native "C" compiler for the 29K processor and runs on the AM29000 coprocessor board	$ 900
7/8" x 11" 1/2" green bar paper (Qty: 3 boxes)	$ 100
ple Imagewriter II printer ribbons (Qty: 12 ribbons)	$ 40
1/2" 800k floppy disks (Qty: 200 floppies)	$ 200
Sub-total	$ 11390

Macintosh IIx Hardware Developement

I. YARC Systems NuSuper Data Acquisition Parallel Interface

Purpose of this time is to design , fabricate and test the parallel interface for telemetry input. This time is also to check-out and upgrade the test equipment to simulate the telemetry frame transmission data.

	Man-Hours
1. Design	16
2. Specification, Documentation & Drafting	32
3. Fabricate	8
4. Unit Test and Check-out	16
Sub-total:	72

Macintosh IIx Hardware Developement

I. YAPC Systems NuSuper Data Acquisition Parallel Interface

Purpose of this time is to design , fabricate and test the parallel interface for telemetry input. This time is also to check-out and upgrade the test equipment to simulate the telemetry frame transmission data.

	Man-Hours
1. Design	16
2. Specification, Documentation & Drafting	32
3. Fabricate	8
4. Unit Test and Check-out	16
Sub-total:	72

Macintosh IIx Hardware Developement

I. YARC Systems NuSuper Data Acquisition Parallel Interface

Purpose of this time is to design , fabricate and test the paralliel interface for telemetry input. This time is also to check-out and upgrade the test equipment to simulate the telemetry frame transmission data.

	Man-Hours
1. Design	16
2. Specification, Documentation & Drafting	32
3. Fabricate	8
4. Unit Test and Check-out	16
Sub-total:	72

Macintosh IIx Software Developement

I. User Monitor Interface Task (Main task)

Purpose of this task module is to initialize run-time data regions, perform simple startup diagnostics on the system components, start supporting tasks, download the gray scale stepwedge standard file to the TrueVision image processor, download micro-code into the YARC Systems NuSuper Coprocessor board, perform as an operator interface from keyboard or mouse, monitor and report operation errors to the display screen.

	Man-Hours
1. Design	8
2. Specification & Documentation	16
3. System and Unit Test Plans	16
4. Coding	24
5. Unit Testing	8
6. System Testing	8
Sub-total:	80

II. Truevision Image Processing Task

Purpose of this task module is to display the gray scale level stepwedge standard and the telemetry pixel data loaded into the on board memory by the User Monitor Interface task or YARC Systems NuSuper Coprocessor respectively.

	Man-Hours
1. Design	8
2. Specification & Documentation	8
3. System and Unit Test Plans	8
4. Coding	16
5. Unit Testing	24
6. System Testing	8
Sub-total:	72

Macintosh IIx Software Developement

III. YARC Systems NuSuper Data Acquisition Software

Purpose of this set of software modules is to perform the data acquisition and removal of the pixel data from the telemetry stream. This module transfers the pixel data to the TrueVision image processor's on board memory. This software is resident in the coprocessor board.

	Man-Hours
1. Design	8
2. Specification & Documentation	16
3. System and Unit Test Plans	8
4. Coding	24
5. Unit Testing	40
6. System Testing	16
Sub-total:	112

IV. Turbo Mouse Controller Task (Menus and Display)

Purpose of this task module is to read the trackball and dual mouse switch positions. This task module translates the positions into explicit image display functions for the TrueVision image processor.

	Man-Hours
1. Design	4
2. Specification & Documentation	8
3. System and Unit Test Plans	4
4. Coding	4
5. Unit Testing	4
6. System Testing	4
Sub-total:	28

Macintosn IIx Software Developement

I. User Monitor Interface Task (Main task)

Purpose of this task module is to initialize run-time data regions, perform simple startup diagnostics on the system components, start supporting tasks,download micro-code into the YARC Systems NuSuper Coprocessor board, perform as an operator interface from keyboard or mouse, monitor and report operation errors to the display screen.

	Man-Hours
1. Design	8
2. Specification & Documentation	16
3. System and Unit Test Plans	16
4. Coding	16
5. Unit Testing	8
6. System Testing	8
Sub-total:	72

II. Automatrix Image Analyst Program Modification

Purpose of this task module is to display the gray scale level stepwedge standard and the telemetry pixel data loaded into the Macintosh IIx MACbus memory by the YARC Systems NuSuper coprocessor or from a file on the hard disk drive. Program modification includes displaying an image directly from its memory location.

	Man-Hours
1. Design	8
2. Specification & Documentation	3
3. System and Unit Test Plans	2
4. Coding	3
5. Unit Testing	2
6. System Testing	2

Macintosh IIx Software Developement

III. YARC Systems NuSuper Data Acquisition Software

Purpose of this set of software modules is to perform the data acquisition and removal of the pixel data from the telemetry stream. This module transfers the pixel data to the TrueVision image processor's on board memory. This software is resident in the coprocessor board.

	Man-Hours
1. Design	8
2. Specification & Documentation	16
3. System and Unit Test Plans	8
4. Coding	24
5. Unit Testing	40
6. System Testing	16
Sub-total:	112

Macintosh IIx Software Developement

I. User Monitor Interface Task (Main task)

Purpose of this task module is to initialize run-time data regions, perform simple startup diagnostics on the system components, start supporting tasks,download micro-code into the YARC Systems NuSuper Coprocessor board, perform as an operator interface from keyboard or mouse, monitor and report operation errors to the display screen.

	Man-Hours
1. Design	8
2. Specification & Documentation	16
3. System and Unit Test Plans	16
4. Coding	16
5. Unit Testing	8
6. System Testing	8
Sub-total:	72

II. Automatrix Image Analyst Program Modification

Purpose of this task module is to display the gray scale level stepwedge standard and the telemetry pixel data loaded into the Macintosh IIx MACbus memory by the YARC Systems NuSuper coprocessor or from a file on the hard disk drive. Program modification includes displaying an image directly from its memory location.

	Man-Hours
1. Design	8
2. Specification & Documentation	8
3. System and Unit Test Plans	2
4. Coding	8
5. Unit Testing	2
6. System Testing	2

Macintosh IIx Software Developement

III. YARC Systems NuSuper Data Acquisition Software

Purpose of this set of software modules is to perform the data acquisition and removal of the pixel data from the telemetry stream. This module transfers the pixel data to the TrueVision image processor's on board memory. This software is resident in the coprocessor board.

	Man-Hours
1. Design	8
2. Specification & Documentation	16
3. System and Unit Test Plans	8
4. Coding	24
5. Unit Testing	40
6. System Testing	16
Sub-total:	112

V E N D O R S

Macintosh IIx Computer Quotation	MacFriends, Inc. 10540 South East Stark Portland, Oregon, 97216 Attn: Mike Order Refr. No. 62601 June 27, 1989
Big Picture IQ Display Monitor & controller	E-Machines, Inc. Attn: Tina Local Dealer: Cambridge Electronics 617-625-2525
4 MBytes Extended Memory Board	List $2396 Sale $1430 Second Source 2011 E. 5th Street Suite 6, Tempe , AZ, 85281 Refr: MacWorld ; 2/89 602-966-0357
Magnavox 14" Macintosh II Display Monitor	Retail $509
E-Machines, Inc. Big Picture IQ 17" gray scale monitor with controller	Retail $2599
Kensington Turbo Mouse ADB	Retail $109 Beverly Hills Computer 279 S. Beverly Drive Suite 1200 Beverly Hills, CA., 90212 213-273-3710 800-426-8166 Refr: MacWorld ; 6/89
Imagewriter II dot matrix printer with cable	Retail $450
Apple 13" Color Monitor	Retail $750

V E N D O R S

Macintosh II 8 bit video card	Retail $495 Kiwi Computers P.O. Box 67381 Los Angeles , CA., 90067 213-553-4507
Turbo Mouse (Trackball)	List $170 Kensington Microware Ltd. 800-535-4242 212-475-5200 Dealer Purchase
Image Analyst MacRail	Retail $2000 Retail $4500 Automatix, Inc. 1000 Technology Park Drive Billerica, MA, 617-667-1800 Attn: Steven Rosenfield
TrueVision NuVista 1M Image Display Syster	List $3370
Video Monitor Cables	List $50
Image processing Microsoft C library routines (Source code)	List $50 TrueVision, Inc. 7351 Shadeland Station Suite 100 Indianapolis, IN, 46256 800-858-TRUE (Litr.) 317-841-0332 Local Dealer: Computer Prod. Mktg. Inc 617-969-1152

V E N D O R S

Nusuper Macintosh II RISC Coprocessor System

List $4000

YARC Systems Corporation
5655 Lindero Canyon #721
Westlake Village, CA.,
91362
818-889-4388

Local Representative:

Scheinfein Associates, Inc
174 Haven Street
Reading, Ma., 01867
617-944-2304

32-bit Parallel I/O NuBus Board
Part No. NB-DIO-32F

Retail $595

24-bit Parallel I/O NuBus Board
Part No. NB-DIO-24

Retail $245

Software Drivers for the above boards
Part No. SWB-NLD-M

Retail $295

50 pin Ribbon Cable
Part No. CB-50

Retail $159

Omega Engineering, Inc.
One Omega Drive
P.O. Box 4047
Stamford, CT., 06907
800-826-6342
800-872-9436 (Tech. Info)
203-359-1660

Emerson PC-ET Power Line Conditioner

Emerson Lighting Services
Waterbury, CT.,
203-756-8148
Attn: Richard Smith

V E N D O R S

Fortran 77 (VAX compatible extensions) Retail $500
- includes Apple's MPW development environment
- interfaces to assembly and C programs compatible with the MPW environment

Language Systems Corp.
441 Carlisle Drive
Herndon , VA. , 22070
703-478-0181
Attn: Steve Lavagnino

Lightspeed "C" Compiler for the MAC II in conjunction with the Truevision Inc. image processing board. Retail $200

Mac Warehouse, Inc.
1690 Oak Street
P.O. Box 1579
Lakewood, NJ, 08701
800-255-6227
201-367-0440 (Info)
Attn: Kerry

Apple Computer "C" Compiler for for the Mac II in conjunction with the Automatix, Inc. image processing software. Retail $200

Apple Computer, Inc.

Apple Imagewriter II printer ribbons (12) Retail $3.00 / ribbon

Dayton Computer Supply
1220 Wayne Avenue
Dayton, Ohio, 45410
800-331-6841
513-252-1247

3 1/2" floppy disks (200) Retail $ .89 / floppy

MEI/Micro Center
1100 Steelwood Road
Columbus , Ohio,
43212-3972
800-634-3478

APPENDIX B: ESTIMATE FOR A SCIENTIFIC DATA ANALYSIS AND DISPLAY COMPUTER USING A SUN MICROSYSTEMS SPARCstation 1

Summary

Option #1 ; SUN MICROSYSTEMS INC. SPARCstation 1 with a 1190x900 16" Color 66 HZ. Sony monitor.

1. Computer and related hardware	$ 26400
2. Purchased Software	$ 4945

S u m m a r y

Option #2 ; SUN MICROSYSTEMS INC. SPARCstation 1 computer with a Megatek 1280x1024 XX" Color/Gray Scale monitor.

1. Computer and related hardware	$ 24600.
2. Purchased Software	$ 4945

epared by: M. A. Purinton
vision 0.00.00

July 12 , 1989

tion no. 1 ---------- SUN MICROSYSTEMS INC. SPARCstation 1 with a 1190x900 16" Color 66 HZ. Sony monitor.

H A R D W A R E

n Microsystems SPARCstation 1 computer
- includes 16 Mbytes of DRAM memory
- includes an internal 1.4 Mbytes (formatted) 3 1/2" floppy disk drive
- includes an external 327 Mbytes (formatted) 3 1/2" hard disk drive
- includes an external 150 Mbytes (formatted) cassette tape drive
  - uses the DC300XL cassette tape
- includes floating point RISC processor
- includes mouse and interface
- includes video controller card and cables
- *- includes 1190x900 Color / B&W 66 hz. RGB monitor with 256 gray levels
- includes three (3) S-bus slots
- includes GX graphics accelerator card
  - this item uses two of the three (3) available S-bus slots
  - this item can not be purchased separately ($2K deduct)
- no expansion chassis is available at this time for the S-bus
- no VMEbus interface available
- includes SUNVIEW ; SUN O/S (Unix) ; C compiler ; Libraries and utilities
  - a Fortran 77 compiler is available separately

$ 24000

lett Packard DeskJet printer — $ 1000

lett Packard DeskJet printer cable — $ 235

ergreen Systems International — $ 365
Diamond Workstation Trackball
- includes cable
- includes manual
- additional button over mouse

erson Computer Power PC-ET A.C. line conditioner — $ 800
- 3 A.C. power outlets
- 360-VA output
- noise filtering and spike suppression

Sub-total $ 26400

epared by: M. A. Purinton
evision 0.00.00

July 12 , 1989

tion no. 2 SUN MICROSYSTEMS INC. SPARCstation 1 computer with a Megatek 1280x1024 XX" Color/Gray Scale monitor.

H A R D W A R E

n Microsystems SPARCstation 1 computer
- includes 16 Mbytes of DRAM memory
- includes an internal 1.4 Mbytes (formatted) 3 1/2" floppy disk drive
- includes an internal 327 Mbytes (formatted) 3 1/2" hard disk drive
- includes an external 150 Mbytes (formatted) cassette tape drive
  - uses the DC300XL cassette tape
- includes floating point RISC processor
- includes mouse and interface
- includes video controller card and cables
- includes 1190x900 Color / BW 66 hz. RGB monitor with 256 gray levels
- includes three (3) S-bus slots
- includes GX graphics accelerator card
  - this item uses two of the three (3) available S-bus slots
  - this item can not be purchased separately ($2K deduct)
- no expansion chassis is available at this time for the S-bus
- no VMEbus interface available
- includes SUNVIEW ; SUN O/S (Unix) ; C compiler ; Libraries and utilities
  - a Fortran 77 compiler is available separately

$ 24000

gatek 1280x1024 XX" Color/Gray scale Monitor $ ---------

ulett Packard DeskJet printer $ 1000

ulett Packard DeskJet printer cable $ 235

ergreen Systems International
Diamond Workstation Trackball $ 365
- includes cable
- includes manual
- additional button over mouse

erson Computer Power PC-ET A.C. line conditioner $ 800
- 3 A.C. power outlets
- 360-VA output
- noise filtering and spike suppression

Sub-total $ 26400

SPARCstation 1 Computer Configuration

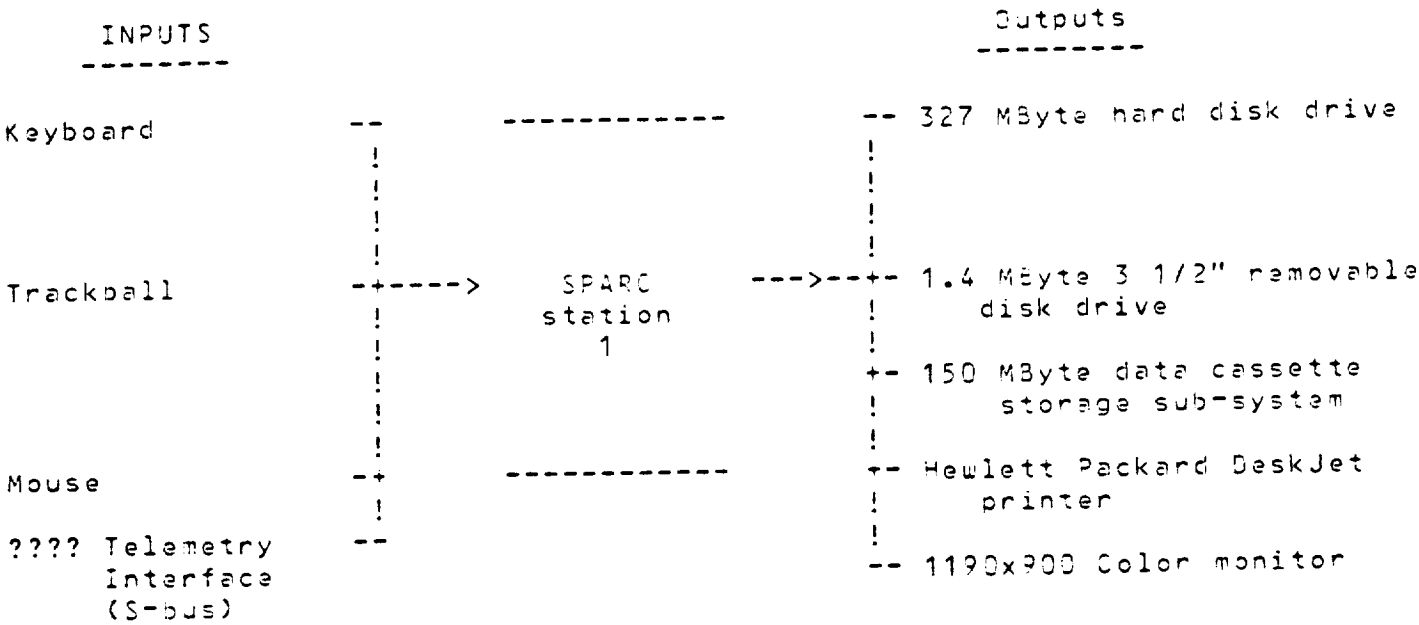

epared by: M. A. Purinton
evision 0.00.00

July 12 , 1989

S O F T W A R E

rtran 77 (ANSI F77 standard)	$ 1200
L Language Compiler for the SUN Microsystems SPARCstation 1 computer	$ 2900
7/8" x 11" 1/2" green bar paper (Qty: 3 boxes)	$ 100
wlett Packard DeskJet Ink Cartridges (Qty: 12 cartridges)	$ 250
wlett Packard DeskJet Font Cartridge (Qty: 1 cartridge)	$ 75
1/2" 1.4MByte floppy disks (Qty: 200 floppies)	$ 200
0 MByte Data Cartridges DC300XL (Qty: 10 data cartridges)	$ 220
Sub-total	$ 4945

APPENDIX C: MEMO CONCERNING PHOTOGRAPHIC CAMERA CHARACTERIZATION AND REFURBISHMENT

SYS-89-95

MEMORANDUM

TO: D. Moses

FROM: F. Hills and R. Schueller

SUBJECT: Test of Two Flight Film Cameras

DATE: 11 Sept. 1989

CC: P. Bjorkholm, R. Eng, T. Fillion, R. Gaillardetz

A number of tests were performed on the two solar rocket flight film cameras to determine what was causing the malfunctions that have been observed. The conclusions are:

1. The film splices should be taped on both sides of the film not just the emulsion side as has been the practice in the past. With the tape on only the emulsion side the film tends to separate from the splicing tape as it rounds the supply sprocket and catches the shoe that holds the film in contact with the sprocket. This caused the splice to break in one case, and to mutilate the sprocket holes in another case. Out of 39 tests these two were the only cases in which the film was badly damaged.

2. The film is not advanced across the platen by the pawl reliably. This failure is noted by a change in the size of the film service loops on the supply and take-up sides of the platen. The total length of both loops remains the same, but the loop on the supply side will increase at the expense of the loop on the take-up side.

This failure was observed on both cameras with the SO-212 film and on camera #1 with the Technical Pan 2415 (TP-2415). It occurred at any place on the film not just at splices.

The cause of this failure could be any of the following properties:

A. The fingers on the pawl that engage the sprocket holes of the film have been rounded by wear.

B. The play in the pawl in the direction of engaging the sprocket holes is too much.

Both of these properties are worse on camera #1 and this camera fails this advance much more often than does camera #2.

C. The pressure the platen exerts against the film to hold it on the pawl fingers may be incorrect.

D. The flexibility of the thin SO-212 must be part of the problem, for the fingers of the pawl penetrate a slot in the platen that should prevent the film from slipping off the ends of the fingers. The excessive play in the pawl of camera #1 permitting the film to fall off the end of the fingers is the most likely explanation for this failure with the TP-2415 film.

3. Another problem is the shrinking of the size of both service loops. For this to occur the supply sprocket must stop driving film into the supply service loop while the take-up sprocket or the take-up reel drive removes film from the service loops. Since the supply and take-up sprockets are geared together the film must become disengaged from the supply sprocket for this to happen. In the tests this failure occurred only once and it appears that the film became disengaged by the web between sprocket holes being torn out. This may not be the complete explanation. See test 2 below.

The film could also become disengaged if it were shifted laterally so that the sprocket holes do not line up with the teeth of the sprocket. Two properties of the splicing device were observed that might cause this lateral shift. In some cases the splicing device had trimmed the splicing tape so that it extended beyond the edge of the film. In another case the two pieces of film at the splice were offset laterally from each other. A shifting of the film may be an explanation for past observed failures of this type where there was no damage to the sprocket holes.

4. Scratch tests were made where film was run through the camera, developed, and examined for scratches made by the camera.

A. Film camera #1 has problems with scratching the film. The locations of the most prominent scratches are: Three at 0.378", 0.456", and 0.745" from the bottom edge and three at 0.212", 0.231", and 0.487" from the top edge.

B. Film camera #2 produces scratches on the film. The locations of the most prominent are: a region 0.285" wide centered on a line 0.688" from the top, and a single scratch 0.232" from the top edge.

C. The position of the exposures on the scratch test film provided more information about the miss-advancing of the film. As would be expected there was some frame overlap when the film was miss-advanced by the pawl. The film from camera #2 shows this behavior. However, this can only be so for the first few misses. As the pawl fails to advance the film sufficiently, the take-up service loop shrinks in size. Eventually the film pulls tight on the take-up side and the take-up drive sprocket will move the film if the pawl does not (since there is no longer any slack on that side). On the film from camera #1 there are quite a few miss-advances beyond the point where the service loop would have pulled tight. In addition, there are unexposed areas where it appears that the film was moved more than should be possible. These were, at

first, thought to be very short exposures made when the film was advanced with the push button controller. However, in a test in which the computer controlled the exposures even the shortest possible exposures were fully exposed.

An investigation has produced a possible explanation for some of the behavior of camera #1, but not all (see scratch test below).

5. The computer control of the cameras was checked under most combinations of the following: four different supply voltages
with and without film
with and without the shutter sensor switch enabled
with and without the filter sensor switch enabled
with and without the correct initial filter position

with a variety of exposure sequences.

In these tests with camera #2 all exposures were made with the correct filter in position. There was one loss of the take-up service loop.

In these tests camera #1 performed almost as well with the filter position, but there were 29 losses of the take-up service loop.

These results and the fact that the filter-wheel, the sprockets, and the pawl are all operated by the same gear mechanism show that the failures with the film are mechanical problems associated with the coupling between the film and the sprockets and pawl, and are not due to the timing of the electrical pulsing of the camera clutch.

Camera #1 failed to position the filter only under the fastest speed conditions (i.e. maximum voltage, no film load, and maximum programmed rate of filter change) and with the shutter switch disabled. The reason for this failure was found to be that the release time of the clutch was twice that specified by the manufacturer. This seems to be caused by the spring tension on the clutch release being too weak.

6. The manufacturer's specification for the minimum time the clutch should be energized and de-energized is 25 msec. for both times. In the solar rocket the computer energizes the clutch until it senses that the shutter is closed which guaranties that the clutch has been energized long enough. Because of this the times change depending upon the supply voltage and the film load in the camera.

Should the shutter sensor fail, the computer will energize the clutch for a default time.

The following are the times measured for the two cameras at the lower (26 volts) and upper (32 volts) limits of the supply voltage expected during a flight. These values may change depending upon how the cameras change during refurbishment.

Camera #1

With a supply of 26 volts and a film load

Energize time = 21 msec.
De-energize time > 73 msec.

Default

Energize time = 24 msec.
De-energize time > 73 msec.

With a supply of 32 volts and no film load — Energize time = 18.5 msec.
De-energize time > 56 msec.

Default

Energize time = 24 msec.
De-energize time > 46 msec.

The de-energize times meet the specification, but the energize times do not. The short energize times show that the clutch can be engaged with a pulse much shorter than 25 msec. This and the fact that the clutch does not disengage fast enough at high speed, even at these long de-energize times, indicates that the tension of the return spring on the clutch release is too low. Although the tension can be adjusted the spring looks as if it has been stretched and should be replaced.

The default energize time was that found to be required for proper operation at high supply voltage.

Camera #2

With a supply of 26 volts and a film load
Energize time = 34 msec.
De-energize time > 70 msec.

Default

Energize time = 35 msec.
De-energize time > 67 msec.

With a supply of 32 volts and no film load — Energize time = 28 msec.
De-energize time > 52 msec.

Default

Energize time = 35 msec.
De-energize time > 47 msec.

These values meet the specification.

7. Besides those above, the following problems with the splicing device were noted:

A. The film cutter works poorly. The cuts may not be square or straight and in one case a feather more than half the width of the film and attached near the side of the film was left.

B. The mating of the two pieces of film at the splice was bad. This could be due to the cutting or to the alignment pins that hold the film during cutting and taping. Splices were noted with spaces between the two pieces of film, some uniform some not. Splices were noted where one film overlapped the other. Sometimes the leading film would overlap the trailing film which would protect against failure type 1 above. Sometimes the opposite would be true enhancing the likelihood of failure type 1. Sometimes the leading film overlapped the trailing film for part of the splice and the opposite for the rest of the splice.

8. Some of the film reels are bent and do not allow the free flow of the film from them.

9. A spacer is needed on the end of the filter-wheel shaft of camera #1 when the colored filter-wheel is used. Without the spacer the screw that holds the filter-wheel in place can be tightened enough to cause a load on the camera. There is no problem in this respect with the flight filter-wheels.

10. The filter-wheel cam of camera #2 does not give a reliable indication of the wheel position. The slot in it is too wide.

11. The cam of camera #1 needs repair from the last flight.

The following is a brief description of tests performed.

1. Test of the movement of film by the camera.

A. A film pack was made of alternating sections of SO-212 and TP-2415 starting with SO-212. The splicing tape was applied to the emulsion side of the first two splices and to the back of the last two splices. In making splices 1 and 3 the splice tape was rubbed with a finger to smooth the adhesion between tape and film after the splicer was used to punch the sprocket holes and trim the tape. In making splices 2 and 4 just the pressure of the punch and trim action of the splicer was applied to the tape. A splice of this latter type may have contributed to the breaking of a splice during the last flight.

This pack was run in camera #2 using the exposure sequence of the last flight. No problems occurred. It was decided that this was not a good test because all the splices would not pass the platen during the rapid advances of the film in the flight sequence as was the case when the flight problem occurred.

B. A film pack was made of alternating sections of SO-212 and TP-2415 starting with SO-212. The length of each section was made so that a splice would pass

the platen in the middle of the fast exposures of a new sequence described below. The first six splices were with tape on the emulsion side, the next two with tape on the back side, and the last splice with tape on both sides.

The new sequence was nine sets of: four 1/4 sec. exposures followed by a 1 sec. exposure.

This pack was run in camera #2.

An analysis after the run indicated that the second splice had somehow caused the film to jam in the supply sprocket, the pawl and take-up sprocket removed the service loops, and eventually pulled the jam free so the film could advance to the end. On this assumption we proceeded with further tests.

A more thorough examination of the film after the tests indicates that something much more complex and not completely explainable occurred. At the second splice the trailing film SO-212 caught in the shoe at the supply sprocket and the corners of the SO-212 were bent over. The lower sprocket holes show that the pawl pulled at the film hard enough to crush the edge of the holes indicating the film was jammed. A count of the sprocket holes from the crushed holes back toward the splice, assuming no supply service loop, would put the splice in the sprocket, but after the beginning of the shoe where the film would catch. The film could have been caught in the slots of the shoes that the sprocket teeth move in. However, the torn and creased sprocket holes that indicate where the film could have been in the sprocket without the sprocket advancing it are further back, and could not have been in the sprocket if the film was jammed by the splice. There are some fold marks in the film between the splice and the torn sprocket holes. One might think that the film could have been jammed after the supply sprocket causing the sprocket to tear the holes. But, a count of the sprocket holes shows that the jam would have been in the middle of the service loop away from all obstructions.

The damage to the sprocket holes on the remainder of the film appear to be due to the pawl advancing the film with no service loops.

Tests C, D, and E below were devised to determine the effect of the following on the camera failures: film types, the placement of the tape on the splice, the number of layers of tape on a splice, and the mating edges of the film pieces spliced.

C. A film pack of SO-212 with no splices was run in camera #2 with the new sequence. The film load indicator failed between the fifth and sixth 1 sec. exposures. The service loop shifted to the supply side. No sprocket holes were damaged.

The film was cut and spliced with the tape on the emulsion side, and run again. No failures were noted. Just cutting the film guaranteed matching ends of film to splice.

The splice was cut out with two cuts, possible mismatched film ends, spliced again with tape on the emulsion side, and run. The film load indicator failed

at the seventh 1 sec. exposure. The service loops shifted to the supply side. No sprocket holes were damaged.

Tape was added to the back of the splice, and run again. The film load indicator failed between the fifth and sixth 1 sec. exposures. The service loops shifted to the supply side. No sprocket holes were damaged.

The test above was repeated twice. There were no failures on one. The service loops shifted to supply side on other.

Tape was added to emulsion side of splice and run again. There were no failures.

At this point the film was marked so that the position of various frames of the film could be observed through the aperture of the camera during the test. The following frames were marked: the frame to be in the aperture when the film was loaded, the frames to appear in the aperture after each of the five preliminary advances, and the frames at the 1 sec. exposures. These marks showed when failures of type 2 occurred. Also, six points along the service loops were marked after the film was loaded, after the preliminary advances were made, and after the sequence was run. Counting the sprocket holes between these marks showed more exactly any changes in size of the service loops.

Over the course of the tests this marked film pack was run an additional eight times. In three of these runs the supply service loop increased in size, but the total size of both loops remained the same. The loops were ok in the other five runs. No sprocket holes were damaged in any of the eight runs. In one of these runs the camera was operated aperture up in which position the pawl tended to fall into the sprocket holes during the return portion of the pawl motion. This was done to see if the pawl was advancing the film correctly, but driving it backward during the return motion. No failures were noted on that run, and thus indicate no problem with the pawl return motion.

D. A series of tests like those in C above were performed using TP-2415 film in camera #2. In all seven runs were made with no failures.

E. A series of tests like those in C above were performed using a film pack starting with a strip of SO-212 spliced to a strip of TP-2415 in camera #2. In all four runs were made with no failures.

The results of tests C - E indicate that the shifting of the service loop failure occurs with the SO-212 film and may occur any place not just at splices.

F. A film pack like that in test B, except that all splices had the tape on the emulsion side and the film was marked as in test C, was run in camera #2 with the new sequence. The film broke at splice 6 in the supply sprocket. The film was found in the sprocket at a 45 degree angle, with only the top sprocket hole at the splice engaged in the sprocket. There were no crushed sprocket holes in the film preceding the splice, so the pawl did not have to pull hard when the break occurred. It is in this film pack where the problems in the splices were noted.

G. A film pack like that in test B, except that all splices had tape on both sides and the film was marked as in test C, was run in camera #2 with the new sequence. There were no failures in five runs. This indicates that the tape should be applied to both sides of splices.

H. Ran film pack D in camera #1. There were no failures.

I. Tried to run film pack C in camera #1. The service loops shifted to the supply side on the first preliminary advance of two trials. It was here that the large play in the pawl of camera #1 was found.

2. Film Camera Scratch Test

A. Both rocket film cameras were tested by running SO-212 film through a series of exposures manually. Approximately six feet of film was used in each test. The film was allowed to run off the supply reel and wind up on the take-up reel. The room lights were left on such that each frame would be exposed to some degree.

The film was developed in the Enterprise Photo Processor using HC-110 at dilution D at 23°C for 3 minutes. It was washed carefully while submerged to remove the carbon backing, then soaked in Kodak Photo-Flo 200 and hung to drip dry. No method was used to remove the excess Photo-Flo to avoid scratching the film outside the camera test.

a. Film Camera #1

Two problems are readily evident on this film strip.

The first and most obvious is the irregular spacing of the frames on the film. There are overlapping frames where it appears the pawl has not moved the film far enough to separate the frames. And there are unexposed spaces between some frames of various sizes, from under 1 sprocket hole wide to 5 holes wide (a frame is 4 holes wide). The normal spacing is a small fraction of a hole wide. It was initially thought that the unexposed spaces were do to very short exposures for the spaces as wide as a frame, and a combination of short exposures and miss-advances for the spaces narrower than a frame. This was proved incorrect in a later test, see below.

At first thought, the miss-advances seem to be explainable by considering the pawl's demonstrated inability to move the film reliably. This can only be so for the first few misses. As the pawl fails to advance the film sufficiently, the take-up service loop shrinks in size. Eventually the film pulls tight on the take-up side and the take-up drive sprocket will move the film if the pawl does not (since there is no longer any slack on that side). On the film from camera #1 there are quite a few miss-advances beyond the point where the service loop would have pulled tight.

A few of the faulty advances are summarized below.

FRAMES	PROBLEM
1 ---> 2	1 sprocket hole (accountable by initial set up)
7 ---> 8	not fully separated : frames are touching
9 ---> 10	more overlap than above
10 ---> 11	normal spacing
11 ---> 12	still more overlap
16 ---> 17	large spacing (greater than normal)
17 ---> 18	large spacing
18, 19, 20	all overlapped
20 ---> 21	large spacing
21, 22, 23, 24, 25, 26	all are overlapped
26 ---> 27	normal spacing

The second problem is scratching of the film. There is a scratch located 0.453" up from the bottom edge of the film. This scratch starts near the beginning of the film after a few of the miss-advances occurred. This could be where the take-up service loop pulled tight. The scratch grows more pronounced as more miss-advances occur. The scratch becomes sharper at the center of the film and then fades to a dull wide scratch at the end of the strip. Additional scratches occur from 0.510" to 0.394" from the bottom edge of the film and cover what is the lower quarter of the image. Two other scratches are located near the top of the film 0.213" and 0.235" from the top edge. These start at the beginning of the exposure sequence and continue with no variations to the end. They are in the top portion of the image by about 0.030". There was, also, a scratch 0.487" from the top.

Some of these scratches could have been caused by the film coming in contact with something it normally would not, when the take up service loop shrank.

b. Film Camera #2

The film strip run manually through camera #2 does not show any visible scratches. The exposures are very dark such that any evidence of scratches on the frames themselves would be lost. The spaces between frames is very small so detection of a scratch would be difficult. These regions were viewed under a magnifier with the film illuminated by a light table. No scratches were seen this way.

There were also some miss-advances. These were located at frames 23 ---> 24, 34 ---> 35, 65 ---> 66. The miss-advances in film camera #2 can be attributed to the pawl not advancing the film correctly, since there were only three miss-advances found.

There were no large spaces between any of the 90 frames in the sequence.

B. To make a better check for scratches another test was performed on both cameras where the exposures were computer controlled using the sequence of flight 36.038CS, but under no light conditions by putting a piece of tape over the aperture. Also, a longer film strip was used, so the film would not run off the supply reel, and the service loops could be checked after the test.

a. The film from camera #1 showed the scratch 0.456" from the bottom edge was still present as well as the two scratches 0.212" and 0.231" from the top edge. A new scratch was observed toward the end of the strip 0.745" from the lower edge (center of the frame) as well as an intermittent scratch under the marks 0.378" from the bottom edge. The service loops did not shrink during this test, hence, these scratches were most likely caused by a part of the camera that touches the film normally (like the front aperture plate).

This film shows another problem with camera #1. Groups of three exposure marks (sometimes four) were observed along the film. The groups were in a line and spaced 1.465" center to center. They seem not to be caused by a light leak, however, for a different number of marks appear in successive frames. There would be one mark in a frame, two in the next frame, then back to one in the next frame, and so on. No explanation for this has been found.

b. The film from camera #2 showed scratches on the film. The locations of the most prominent are: a region 0.285" wide centered on a line 0.688" from the top, and a single scratch 0.232" from the top edge. The service loops did not shrink during this test, hence, these scratches were most likely caused by a part of the camera that touches the film normally.

C.To check the short exposure hypothesis of section 2.A.a. above, another test was performed on camera #1. The exposures were computer controlled using the sequence of flight 36.038CS. The test used the room lighting to expose the film as was done in the manual test. Also, a longer film strip was used, so the film would not run off the supply reel, and the service loops could be checked after the test. The results were that even the shortest possible exposures (i.e. those made as the camera bypassed the unused filter positions between exposures) were fully exposed. This seem to indicate that in the manual test the film was advanced more than is possible. Unfortunately, during the computer test no over-lapping frames occurred, and thus does not show what would happen during a failure.

D. The operation of the camera was investigated to determine if there is any way for it to make a partial advancement of the film. The proper operation of the camera is as follows. The clutch that causes the camera to be advanced is held by a latch. when the latch is withdrawn, the clutch is free to turn and is turned by the motor. When the latch is inserted, the clutch turns until it stops against the latch. Thus, the clutch turns by one or more full rotations. Nothing stops it after part of a rotation. The film drive sprockets are geared directly to the clutch and advance the film one frame (4 sprocket holes) for one rotation of the clutch. One sprocket adds film to the supply service loop. The other removes film from the take-up service loop. A shutter and a filter-wheel are also geared directly to the clutch. One rotation of the clutch rotates the shutter once, and the filter-wheel one filter position (one fifth of a rotation). The shutter is a circular disk with a notch in it that is a little less than a quarter of the circle. When the camera is stopped, the notch is in front of the film, producing exposure. When the clutch is released, the shutter covers the film during the first quarter turn (actually

the first eighth turn), and uncovers the film during the last quarter turn (actually the last eighth turn). During the middle half turn a pawl advances the film across the platen one frame (4 sprocket holes). The relationship between these actions is important, for it guarantees that the film will not be exposed while it is being moved, and vice versa. The pawl removes film from the supply service loop, and adds film to the take-up service loop. The non-linear drive of the pawl is directly geared to the clutch.

Only two abnormal operations have been found to explain any of the failures of the cameras.

a. The first, is the film slipping off the pawl fingers which will cause a miss-advance of the film in front of the platen.

b. The second is as follows. Consider the case where the take-up service loop has no slack. On the next advance the following will happen. During the first quarter turn the film will be advanced across the platen one sprocket hole by the take-up sprocket. The pawl, if the holes line up properly, would then advance the film across the platen four more holes. This is a total advance of five holes across the platen. At the last four holes the next exposure will be made. At the first hole only a very short exposure will be made as the shutter closes and the film advances at the same time. The sprockets during this advance will move the film four holes. Thus, the supply service loop will loose a hole and the take-up loop gain a hole.

This action explains how a one hole non-exposed space can occur between frames. It also shows how further miss-advances can occur after the take-up service loop has pulled tight. However, the resulting frame overlap could be only one hole. Non-exposed spaces and frame overlaps of this size were on the manually advanced film from camera #1.

A check of the shutter, that closes as the film is advanced, showed that it is tightly connected to its shaft, and does not seem to have slipped. How the large unexposed spaces occurred is not known.

3. Computer Control of Cameras

These tests checked the computer control of the cameras. The cameras were run through a programmed sequence of exposures and filter positions. A visual comparison of the actual filter sequence and the programmed sequence indicated any errors that may have occurred in the operation of the camera. This is the full operation of the camera, for the film advancing sprockets and pawl are geared together with the filter-wheel.

Two of the conditions the camera must operate under are discussed below. Because the battery supply voltage changes over a flight all the tests were performed under each of the following voltages:

26 volts	lower bound on the supply voltage
28 volts	nominal supply voltage
30 volts	
32 volts	upper bound on the supply voltage.

Because pre-flight testing is done without film all the tests were performed with and without a film load (TP-2415 was used).

A. Normal operation

The cameras were run through the flight 36.038CS exposure sequence under the eight combinations of voltage and film load above. The correct filter sequence was observed for both cameras in all combinations.

B. Simulated failure of the shutter and filter sensing switches

These were same tests above, except the shutter and filter switches were disabled. The correct filter sequence was observed for both cameras in the eight voltage and film load combinations.

C. Correct the filter

If the computer and the camera filter number get out of synchronization, they will be realigned when the computer senses the camera passing filter #1. To test this operation a two exposure sequence was programmed. The first exposure had the filter to test. The second exposure had an erroneous starting filter. The sequence first tests for the advance to the proper filter, and then resets the filter-wheel to the erroneous starting filter for the next run of the test. The following is a table of the starting and test filter pairs that were tested. Until it finds otherwise the system assumes it is started at filter #1.

Start	Test	Filter Arrived At	Comment
1	3	3	Correct starting filter
3	3	5	Computer assumes camera starting at 1 and needs to advance two filter positions to get to 3, thus, advances to 5. Filter-wheel does not pass filter #1, hence, computer does not detect the error. The error is corrected on the advance to the starting filter.
4	3	3	Computer assumes camera starting at 1 and needs to advance two filter positions to get to 3, thus, advances to 1. At 1 the computer detects the error and advances the filter to 3.
5	3	3	Computer assumes camera starting at 1 and needs to advance two filter

			positions to get to 3, thus, advances toward 2. As the filter-wheel passes 1 the computer detects the error and advances to 3.
1	1	1	Correct starting filter
2	1	1	Computer assumes camera starting at 1 and needs to advance five filter positions to get to 1, thus, advances toward 2. As the filter-wheel reaches 1 the computer detects the error and stops the advance at 1.
5	1	1	Computer assumes camera starting at 1 and needs to advance five filter positions to get to 1, thus, advances toward 5. As the filter-wheel reaches 1 the computer detects the error and stops the advance at 1.

Both cameras were tested with each of the above start and test filter pairs ten times at all eight combinations of voltage and film load. No filter errors occurred. Some losses of the take-up service loop were observed with camera #1 in the tests done with a film load.

D. Correct the filter with simulated failure of shutter sensing switch.

The same tests as in C above were performed except that the shutter sensor switch was disabled. No filter errors occurred. Some losses of the take-up service loop were observed in the tests done with a film load. Most of these occurred with camera #1, but one occurred with camera #2.

E. Measurement of camera clutch energize and de-energize times.

The clutch energize and de-energize times were measured with a scope. The APC (advance photographic camera) command was used to operate the camera to measure the energize time from an initial stopped condition. The manual control was used to operate the camera to measure times from which the de-energize time could be estimated. To measure the times that occur as the camera advances past undesired filter positions between exposures, the camera was controlled by the sequence described in Test 1.B. above. The default time was measured by making the measurements with the shutter sensor switch disabled.

It was during the test with the sequence of test 1.B, at 32 volts, with no film load, and with the shutter sensor switch disabled that camera #1 failed to advance the filters correctly, and the problem traced to the clutch release spring tension.

APPENDIX D: PREPRINT OF JOURNAL PAPER ON RESULTS FROM 36.021CS AND 36.038CS

CORRESPONDENCE BETWEEN SOLAR FINE SCALE STRUCTURES IN THE CORONA, TRANSITION REGION, AND LOWER ATMOSPHERE FROM COLLABORATIVE OBSERVATIONS

Dan Moses[1], J.W. Cook, J.-D.F. Bartoe, G.E. Brueckner, K.P. Dere, D.F. Webb[2], J.M. Davis[3], J.W. Harvey[4], F. Recely[4], S.F. Martin[5], and H. Zirin[5]

Publication No. 41-

E.O. Hulburt Center for Space Research
Naval Research Laboratory
Washington, DC 20375-5000

[1]Bendix Field Engineering Corp., [2]Emmanuel College, [3]Marshall Space Flight Center, [4]National Solar Observatory, [5]Big Bear Solar Observatory

September 1990

Received_____; Accepted_____

For submission to THE ASTROPHYSICAL JOURNAL

ABSTRACT

The American Science and Engineering Soft X-ray Imaging Payload and the Naval Research Laboratory High Resolution Telescope and Spectrograph (HRTS) instrument were launched from White Sands on 1987 December 11 in coordinated sounding rocket flights to investigate the correspondence of fine scale structures from different temperature regimes in the solar atmosphere, and especially the relationship between x-ray bright points (XBPs) and transition region small spatial scale explosive events. We present the coaligned data from x-ray images, maps of sites of transition region explosive events observed in C IV (100,000 K), HRTS 1600 Å spectroheliograms of the T_{min} region, and groundbased magnetogram and He I 10830 Å images.

We discuss the bipolar magnetic regions (BMRs) and He I 10830 Å dark features which are counterparts of XBPs, and emphasize the frequent double ribbon pattern of the He I dark feature counterparts. We present updated results of the analysis of the relationship of XBPs to emerging, stationary, and disappearing BMRs performed by Webb and Moses, which shows that disappearing (flux cancelling) BMRs are the most significant magnetic field counterpart to XBPs.

We find that the transition region explosive events do not correspond directly to XBPs, which are associated with magnetic bipoles often appearing as prominent network elements, and instead the actual corresponding features in C IV observations are in general brighter, larger scale (~20 arc sec) regions of complex velocity fields of order 40 km s^{-1} or less, which are typical of brighter network elements. These C IV features do not reach the ~100 km s^{-1} velocities seen in the C IV explosive events. However, just as He I 10830 Å dark points and magnetic BMRs are not uniquely associated with XBPs, so also there are many similar C IV network features without a corresponding XBP in the x-ray image.

The C IV explosive events appear to be concentrated in the quiet Sun at the edges of strong network, or in weaker network regions. The x-ray image shows a pattern of dark lanes in quiet Sun areas, and the C IV events are predominantly concentrated within a dark lane, avoiding areas of hazy, slightly brighter x-ray emission probably corresponding to unresolved loop systems in this quiet area of the disk. We also find a greater number of C IV events than we would have expected from the results of a disk survey undertaken on the Spacelab 2 flight of the HRTS payload. This is possibly because of the occurence of a particularly rich region associated with the x-ray dark lane in the field of view, and by an extended detection threshhold from better spatial resolution with the HRTS V data.

I. INTRODUCTION

The physical proximity of the Sun currently provides the only opportunity to observe the detailed spatial structure of a stellar atmosphere. Access to UV and soft x-ray wavelengths via space bourne instrumentation opens a window to observation of the three dimensional organization of the solar atmosphere, from the photosphere through the corona, by comparison of structures at different temperatures. Although comparisons of solar features have been made using multispectral observations during previous space missions, notably from the Skylab and Solar Maximum Mission spacecraft, simultaneous high spatial resolution observations of solar fine structures are still difficult to obtain but highly desirable.

Such fine scale features have been observed in the solar atmosphere in the corona and in the transition region. X-ray bright points (XBPs), bright structures at the 10-30 arc sec spatial scale lasting the order of 8 hours (but with more transient periods of activity), have been observed from space by soft x-ray instruments viewing the corona. The EUV HRTS spectrograph, which views transition region and chromospheric plasmas, has observed highly transient fine scale structures down to arc second spatial scales (see review by Cook and Brueckner 1991). In particular, small scale (~2 arc sec) features in transition region emission lines such as C IV 1548 Å and 1550 Å have been observed which show line profiles broadened to the red or blue by 50-400 km s^{-1}, with average lifetimes of the order of 90 s or less (Brueckner and Bartoe 1983; Cook et al. 1987; Dere et al. 1989).

We wanted to know if these C IV explosive events are related to XBPs. Sheeley and Golub (1979) showed that XBPs are composed of smaller active and evolving loops. Could the C IV energetic events be associated with episodes of activity as XBP structures evolved? Krieger, Vaiana, and Van Speybroeck (1971) showed that XBPs are associated with small bipolar magnetic field regions

(BMRs), and Porter et al. (1987) showed that transient small scale brightenings in C IV intensity are also associated with BMRs. Do XBPs and C IV explosive events have a common magnetic origin? The lack of near simultaneous x-ray and EUV observations had left the correspondence between these coronal and transition region fine scale transient features unclear. Furthermore, we wanted to understand the association of these features with cooler atmospheric structures, for example with photospheric magnetic field structures and with possible He I 10830 Å counterparts.

In an effort to study these questions, a collaborative "bright point campaign" of co-observations from ground and space was organized whose primary purpose was to determine the relationship of XBPs, transition region explosive events, He I 10830 Å dark points or other features, and photospheric magnetic structures. Coordinated sounding rocket flights were made by the American Science and Engineering (AS&E) High Resolution Soft X-Ray Imaging Payload and by the Naval Research Laboratory (NRL) High Resolution Telescope and Spectrograph (HRTS) experiment from White Sands on 1987 December 11, with launches at 18:15 UT (AS&E) and 18:45 UT (NRL). The AS&E experiment obtained full disk coronal images over the wavelength range 8-64 Å, emitted by 10^6 K plasmas, with a spatial resolution of approximately 3 arc sec. The HRTS spectrograph slit of 920 arc sec length was rastered in 2 arc sec steps across an approximately 3 arc min wide area in the northeast quadrant, covering a quiet area out to the solar limb. HRTS spectra were obtained of the C IV 1548 Å and 1550 Å lines, emitted by transition region plasmas at 10^5 K. In addition, spectroheliograms covering an area of approximately 920x460 arc sec were taken over a 20 Å passband centered at 1600 Å.

Collaborative groundbased observations were also obtained from Kitt Peak (National Solar Observatory) and from Big Bear Solar Observatory, including magnetograms (NSO/Kitt Peak and BBSO) and He I 10830 Å (NSO/Kitt Peak). HRTS

1600 Å spectroheliograms can be accurately registered with magnetograms, and the slit position of HRTS spectrograms covering the transition region C IV lines 1548 Å and 1550 Å can be accurately placed on the HRTS spectroheliograms. We could then study the correlation of sites of small spatial scale transition region explosive events with the x-ray and groundbased data, and in particular the spatial relationship with XBPs and with the quiet Sun network. In addition, we examined the evolution of the photospheric magnetic field BMRs associated with the coronal XBPs, and the correlation of He I dark points with XBPs. In this paper we present the co-registered observations from the two sounding rocket experiments and the groundbased observations, and discuss their correspondence and interpretation.

II. ROCKET INSTRUMENTATION

In this section we describe the two rocket payload experiments of the bright point collaboration.

(i) The AS&E x-ray payload

The AS&E High Resolution Soft X-ray Solar Astronomy Imaging Payload was flown on 1987 August 15 and 1987 December 11 in participation with the collaborative bright point campaign. X-ray imaging is achieved in the AS&E payload by grazing incidence optics. The primary mirror is a Wolter Schwarzchild design with principle diameter of 30.48 cm and focal length of 144.9 cm. The reflecting surfaces of the mirror are uncoated fused silica. The level of suppression of scattering which is obtained with this mirror material by the reduction in surface roughness results in a point spread function relatively independent of wavelength (particularly in comparison to the earlier Kanigen Skylab S-054 and sounding rocket mirrors). However, the reflectivity of this surface at the grazing angles of the mirror (approximately 1.5 degrees) is

strongly wavelength dependent and defines the decline of the short wavelength response of the system below 30 Å.

Kodak SO-212 film was chosen as the primary photographic film for this flight because of its superior sensitivity with the longer wavelength filter used to image the "cooler" coronal plasma typical of XBPs. The resolution of the combination of the telescope optics and the SO-212 film is limited by the film, and is approximately 3 arc sec. This film was manufactured in 1973 for the Skylab S-054 X-ray Spectrographic Telescope Experiment Program and has since been kept in cold storage. Aging of the film has had little impact on its x-ray response, and advances in the photometric process continue to make this film a valuable resource for x-ray imaging (Moses et al. 1989). Since this film has been used for almost all high resolution x-ray photographic imaging of the solar corona, comparison with prior observations in synoptic studies is greatly facilitated.

In addition to the filtering effect of the reflectivity of the imaging mirror, the x-rays are also filtered by a heat rejection prefilter of approximately 0.15 μ of aluminum and one of two focal plane filters, a 17.5 μ thick beryllium filter with a bandpass of 8-20 Å, or a 1 μ thick polypropylene filter coated by 0.20 μ of aluminum (for visible light rejection) with a dual bandpass of 8-39 Å and 44-64 Å. A series of exposures through each of these filters was made with exposure times of 0.5 s, 1 s, 3 s, 9 s, and 30 s, with an extra 60 s exposure for the December 11 flight. This sequence was chosen to accomodate the dynamic range of coronal x-ray emission, which can vary by a factor of 10^3 from the quiet Sun to an active region and 10^6 for a flare, as well as to provide additional control on variations induced by photographic development (Moses et al. 1989). The x-ray throughput of the instrument with the polypropylene filter is greater than with the beryllium filter for all temperatures of x-ray emitting plasmas. Furthermore, the throughput of the

polypropylene filter is proportionally much greater for low temperature plasma, so that the ratio of flux through the polypropylene filter to the flux through the beryllium filter provides a good plasma temperature diagnostic over the range $1x10^6$ - $2x10^7$ K (Vaiana, Krieger, and Timothy 1973). Since the objective of the collaborative observations is small scale coronal structure, and since such structures are typically cool (1.5 - $1.8x10^6$ K), we used in this paper the longest available exposures through the polypropylene filters. The December 11 60 s exposure is shown in Figure 1.

A collaborative bright point campaign had been attempted previously in 1985 August during the Spacelab 2 flight of the HRTS instrument. At that time an AS&E sounding rocket had been aborted during boost phase by the White Sands Missile Range safety officer. This abort left a contamination coating on the x-ray mirror from the explosives used to destroy the rocket booster. An effort at cleaning the mirror was made before a 1987 August 15 flight which was our next attempt at bright point collaborative observations, now using two sounding rockets. A review of the x-ray image from this flight compared with previous coronal images convinced us to attempt more intensive cleaning.

The second x-ray mirrror cleaning effort used a considerably more vigorous scrubbing action, coupled with particular attention to removing organic deposits during the final sequence of solvent rinses. This cleaning effort was a dramatic success, and the resulting images from the 1987 December 11 flight show details as fine as from any previous soft x-ray image of the solar corona using grazing incidence. We note that recently Golub et al. (1990) have achieved arc second resolution of active region structures on a sounding rocket flight of a payload using normal incidence optics with multilayer coatings, and imaging predominantly hotter plasmas than observed by the AS&E instrument.

To record even the fainter features, an extra 60 s exposure through the thinnest available polypropylene filter was added to the 1987 December 15 flight

exposure sequence. With the added integration time obtained with the 60 s exposure, the threshold emission measure ($\int N_e^2$ dl) for detection of 1.6×10^6 K plasma, typical of small scale coronal structure, became 1.2×10^{25} cm^{-5}.

The contrast of the December 15 image was improved to the extent that dark lanes between regions of diffuse, quiet coronal emission became readily apparent. While these features can be found on review of previous x-ray coronal images, they do not appear so distinctly defined. It is reasonable to conclude that the intrinsic improvement in image contrast of the fused silica mirror, compared to the metal mirrors used in the Skylab S-054 instrument and the earliest sounding rocket flights, coupled with the reduction in scatter achieved by removing contaminants during the cleaning, and the particularly successful pointing stability maintained during the longer photographic exposures, has aided in the recognition of these coronal features, which show (discussed in §VI) an intriguing relationship with transition region explosive events.

(ii) The NRL HRTS experiment

The NRL High Resolution Telescope and Spectrograph (HRTS) instrument was flown as a rocket payload for the fifth time on 1987 December 11 from White Sands. HRTS consists of a 30 cm cassegrain telescope, a broadband spectroheliograph which was tuned to a wavelength region around 1600 Å, a stigmatic slit spectrograph which covered a wavelength range from 1520-1570 Å including the C IV lines at 1548 Å and 1550 Å, and an Hα imaging system. The spatial resolution of the instrument is potentially sub arc second, and in this flight the smallest resolved spatial features in the slit spectrograph and the spectroheliograph are approximately 1 arc sec in size. Slit spectra were recorded by film exposure using Kodak type 101 emulsion, and spectroheliograph images on Kodak type 104 emulsion. The spectrograph slit of length 920 arc sec was rastered in 1 or 2 arc sec steps across an approximately 3 arc min wide area

in the northeast quadrant, covering a quiet area out to the solar limb. In addition, spectroheliograms covering a field of 920x460 arc sec were taken every other raster step of the slit spectrograph.

An example of a spectroheliograph exposure can be seen in Figure 3. The HRTS spectrograph slit passes down the approximate center of the spectroheliograph image, which is obtained from a solar image reflected from the mirrored slit jaw plates. Three fiducial wires cross the image field perpendicular to the slit. The spectroheliograph passband is centered at 1600 Å, with a 20 Å FWHM. The predominant flux source in this passband is the ultraviolet continuum, arising from the solar temperature minimum region (see Vernazza, Avrett, and Loeser 1976, 1981), with the remaining flux contributed by chromospheric and transition region emission lines. From an integration of this passband over a representative quiet solar spectrum from the atlas of Kjeldseth Moe et al. (1976), where we have estimated the continuum level and separated the flux into emission line and continuum contributions, we find that 72% of the flux measured by the HRTS spectroheliograph from this quiet region would arise from continuum emission.

A series of film exposures of length 2.0 s, 1.0 s, and 0.5 s was taken at every other raster step of the slit spectrograph. In practice, the longest 2.0 s exposures have been used. After initially developing a flight film sample, it was clear that the spectroheliograph instrumental efficiency was down by as much as a factor of 10. With the help of Brian Dohne, a chemical developer was devised which optimally brought out the film latent image, effectively boosting the tail and steepening the gamma of the film characteristic curve. Although the developed images had a greater fog level than nominal, the final images were photometrically reliable.

The slit spectrograph on this flight covered the 1520-1570 Å wavelength range. The slit was widened to a 1 arc sec width to bring down the exposure

time and allow more exposures, covering a greater surface area. The resulting spectral resolution was 0.10 Å. This wavelength range contains chromospheric lines of Si I, Si II, C I, Fe I, and other species, and the transition region resonance lines of C IV at 1548 Å and 1550 Å; in addition, the continuum in this range arises from the temperature minimum region of the solar atmosphere. In this paper we discuss only the C IV slit spectrograph observations. An exposure time of 2.4 s was used for the raster exposures, which optimally exposed the C IV lines. An example of the C IV spectra can be seen in Figure 5.

The slit spectrograph was rastered across the solar field by mechanically stepping the slit position. We wanted to raster as wide an area as possible, but with steps small enough not to miss C IV turbulent events in the field. From the size distribution for these events found by Cook et al. (1987), a step size of 2 arc sec was generally used, although one raster with 1 arc sec step size was performed. As noted above, a spectroheliograph exposure was taken with every second raster step. On these spectroheliograph images the slit can be seen displaced in the raster direction in successive images. Optical abberations in the slit spectrograph arise beyond a slit travel distance of approximately 30 arc sec to left or right of the central slit position, and to cover a wide field four individual rasters were made, with the telescope pointing changed between rasters so that no individual raster exceeded 25 arc sec relative to the central slit position. The nominal raster layout had 4 individual rasters of the 920 arc sec long slit in the following pattern: raster 1 (2 arc sec steps, 26 positions); 5 arc sec inter-raster spacing; raster 2 (1 arc sec steps, 21 positions); 5 arc sec inter-raster spacing; raster 3 (2 arc sec steps, 26 positions); 10 arc sec inter-raster spacing; raster 4 (2 arc sec steps, 24 positions). The total width of the pattern was nominally 186 arc sec, or 3 arc min.

III. THE COLLABORATIVE BRIGHT POINT CAMPAIGN

The collaborative observing plan called for a morning launch of the AS&E payload, followed in one half hour by the NRL HRTS payload, both on Black Brant sounding rockets. Each Black Brant was equipped with a Saab S-19 boost phase guidance system. The S-19 allows a wider tolerance for high altitude winds, and gives a lower dispersion in the re-entry trajectory and final landing spot of the rocket and payload. The morning launch time was chosen to allow groundbased observations at Kitt Peak and Big Bear Solar Observatory to begin an hour or more before launch, while still keeping the actual flight within a time period which would typically insure good seeing at the groundbased observing sites. Observing programs at the groundbased sites were developed which emphasized He I 10830 Å images and magnetograms from Kitt Peak, and videomagnetograms and Hα from Big Bear. At Kitt Peak, full disk images were taken outside the actual flight period, while during the flight period a 512x256 arc sec field at the plannned position of the HRTS field was observed in He I 10830 Å. At Big Bear, a program was devised where videomagnetograms and film Hα images were taken during the observing day in overlapped boxes which also covered the planned HRTS field, while other areas of the Sun where magnetograms showed bipolar regions were also occasionally observed to further support the full disk field of the AS&E x-ray payload.

This planned program was actually attempted several times during the summer of 1987, but was unsuccessful because of difficulties in launching the first rocket because of malfunctions with the S-19 rocket guidance system. On 1987 August 15 the AS&E rocket was succesfully launched, but one half hour later the NRL rocket could not be launched because of a similar S-19 malfunction.

Finally on 1987 December 11 both rockets were succesfully launched. This time, however, another malfunction occurred which affected the pointing of the HRTS payload. Pointing information on pitch, roll, and yaw for the Lockheed

SPARCS payload pointing system is uplinked by radio to the rocket after launch, and a data dropout occured during the sending of the roll angle. Instead of the desired pointing in the southwest quadrant, covering an area which included an active region at the limb, the roll received put the pointing almost 180° away, in the northeast quadrant, with HRTS observing one of the quietest areas on the disk. This did not affect HRTS comparisons with the x-ray image, which is full disk, but precluded comparisons with the highest temporal resolution groundbased observing programs targeted at the planned area in the southwest quadrant of the solar disk. In this paper we illustrate full disk groundbased Kitt Peak observations which are not genuinely simultaneous with the HRTS observations. In Table 1 we summarize the observational material which we discuss in the present paper.

IV. COALIGNMENT OF THE OBSERVATIONS

We have coaligned the full disk images which were obtained: the full disk Kitt Peak magnetograms and He I 10830 Å images, and the x-ray image. We have processed digitized full disk data obtained hours before or after the rocket flights by computer to produce an image rotated to the time of flight. Solar rotation near disk center is 9 arc sec an hour, and in comparing observations hours apart, as we have, where we are trying to determine correspondences in features which may be only arc seconds in dimension (the C IV explosive events, for example), solar rotation is a significant effect. This is purely a geometrical correction, and does not account for actual temporal evolution of features between the time of the actual observation and the time of the rotated image. In addition, no attempt is made to further adjust the numerical values of the constructed image pixels for the changed line of sight, so for example a constructed pixel in a magnetogram will have assigned a magnetic field value from an area of the actual observed magnetogram eastward or westward of this

position, with a different line of sight angle. The Kitt Peak magnetogram and He I 10830 Å images are obtained by the same telescope, and at the same scale, nominally 1 arc second per pixel. The He I image is surrounded by a bright ring at the limb from limb brightening in this chromospheric line. As a check, we verified that the magnetogram limb falls at the inside of this white band on the He I image, as should the limb from a photospheric line.

The general problem of coaligning images from different instruments can be difficult. Besides the obvious necessity to place images on a similar linear scale and rotational orientation, there are often instrumental aberrations present so that to some extent one image is not flat field, perhaps in a nonlinear barrel sense. We developed a computer program to align two images where a number of corresponding fiducial points on each image are believed to exist. This program constructs a rescaled, rotated image from one of the original images which in a least squares senses produces the best coalignment of the selected pairs of fiducial points on each original image. The rescaling can be either linear or nonlinear in x and y.

We coaligned the full disk x-ray image using this program, where as fiducial points we took XBPs and their plausible He I dark point counterparts, or other pairs of fiducial features at small spatial scale which appeared to be plausible counterparts. Although subjective to some extent, this was very straightforward to accomplish. We then checked the resulting aligned x-ray image's limb with the limbs of the Kitt Peak He I and magnetogram images. The x-ray limb, black where sillouted against the brighter general off-disk coronal emission, fell at the magnetogram limb and the inside of the limb brightening ring at the He I limb.

XBPs were identified on the full disk image by the three authors experienced in analysis of the AS&E x-ray data (JMD, DM, and DFW) using a second generation internegative (Haggerty et al. 1975) enlarged to a solar diameter of

10.8 cm, viewed on a light table. The primary image for this purpose was the 60 s exposure taken through the polypropylene filter. The technique was as close as possible to that used in previous investigations of XBP distributions. Issues of counting variations and background bias are discussed in detail by Golub, Krieger, and Vaiana (1976). A comparison with shorter exposures was made to verify that the XBP distribution with exposure time was consistant with previous work. Difficulties in the identification of XBPs include the variation in background exposure in different areas, for example from a coronal hole to the edge of an active region; the variation in intensity from the disk to the limb due to increasing line of sight, which can confuse identification; and the evolutionary development of XBPs from a diffuse and dim object at birth to a bright object with a sharply peaked core during the flaring of an XBP.

The coalignment of the restricted 920x460 arc sec field of view of the HRTS raster to the full disk images was accomplished using the HRTS 1600 Å spectroheliograms. The method is to coalign HRTS V spectroheliograms, which image a wavelength interval around 1600 Å where flux is emitted predominantly from the temperature minimum continuum, with groundbased magnetograms. The T_{min} images are highly correlated in their fine structure with magnetograms (see Cook, Brueckner, and Bartoe 1983), and in fact we can coalign the HRTS spectroheliograms to the Kitt Peak magnetogram to around 5 arc sec accuracy. The HRTS spectrograph slit can be seen on the HRTS spectroheliograph images, and the location of transition region C IV explosive events from the spectra can be accurately transferred to the spectroheliograms, and thus to the magnetograms and the groundbased data.

Individual explosive events were identified on the flight exposures. We measured the position along the slit, using the three fiducial wires as a reference scale, of events with a spatial size along the slit of less than 10 arc sec which showed widened profiles of at least 50 km s^{-1} to either the red or

blue. Selection was done by eye, and becomes increasingly subjective for the faintest events. We estimate our error in determining the position along the slit as 5 arc sec. In addition to the distance along the slit, we also measured the slit position of the limb of the Sun as a marker of an absolute solar position.

As described earlier, a four part raster observational sequence of slit movements and exposures was pre-programmed, where the telescope pointing was changed by command from the ground to separate the individual rasters. We checked the actual position on the Sun of the slit positions, as shown by the slit image on the spectroheliograms, and corrected our preliminary map of C IV explosive event sites based on the nominal planned execution, for both the raster widths and positions observed on the spectroheliograms, and for a general drift along the slit during the observations which was found from the solar limb positions along the slit which we had measured. The limb position is plotted on our C IV explosive events map for comparison with the limb position on other images. The three fiducial wire positions are also plotted on the map.

V. CORRESPONDENCE OF XBPs WITH MAGNETIC BMRs AND He I FEATURES

We will first discuss the comparison of XBPs with bipolar magnetic regions in photospheric magnetograms, and with dark features observed in He I 10830 Å images. An analysis of the correspondence of XBPs with emerging, stationary, and disappearing magnetic bipoles is presented which updates the association of XBPs with disappearing magnetic flux found by Webb and Moses (1990), and a statistical study of the correspondence of XBPs and He I dark points is presented.

(i) XBPs and Magnetic Field BMRs

The association of XBPs with bipolar magnetic regions was made almost immediately after the discovery of XBPs in the first high resolution images of

the x-ray corona (Krieger, Vaiana, and Van Speybroeck 1971). This association of XBPs with BMRs is clear in the 1987 December data, but while a BMR counterpart is always present with an XBP, in fact most BMRs are not associated with an XBP.

The BMRs associated with XBPs also correspond to features in the HRTS 1600 Å images of the temperature minimum region. In Figure 3, the strongest XBP in the HRTS field is seen to correspond in the 1600 Å spectroheliogram to a bright network element. The reason, however, is simply that the brightness temperature of network elements at 1600 Å is linearly related to the absolute value of the underlying photospheric magnetic flux (see Cook and Ewing 1990), and XBPs are associated with strong bipoles. Network elements associated with a magnetic bipole of opposite polarity fields, or with a unipolar element of the same total absolute value of flux, will have similar brightness temperatures at 1600 Å. But while the T_{min} region of the solar atmosphere responds to absolute value of magnetic flux, XBPs are magnetic bipoles, and only the 1600 Å network elements overlying magnetic bipoles could have associated XBPs. In a similar way, the weak He I 10830 Å absorption features map out the network, and strong network elements can have He I counterparts which could be identified as He I dark points. But only those He I dark points corresponding to a magnetic bipole could have in addition an XBP counterpart. We will return with greater detail to the subject of the correlation of XBPs to He I structures in the next section because of the extent that some investigators have used compact He I features as proxies for XBPs.

Since the lifetime of XBPs is short (of order 8 hours), the early evolution of the XBP magnetic structure may be as important in the understanding of XBP dynamics as the simple bipolar geometry of the field. In quiet network regions, magnetic flux appears to emerge in small bipolar ephemeral regions, spread apart with time, and disappear either by gradual fading of the two opposite polarity

elements of the ephemeral region, or by cancellation of one element with another existing opposite polarity element with its own previous evolution as an internetwork element, active region remnant, or ephemeral region (see Martin and Harvey 1979). A time series of magnetograph observations over several hours is necessary to classify a magnetic bipolar region as either (1) an emerging flux ephemeral region, (2) a disappearing flux cancellation, or (3) a stationary flux element lasting an appreciable time, perhaps simply fading with time.

Early work on Skylab data suggested that XBPs are characterized as emerging flux regions (Golub et al. 1977; Golub 1980). Later work with improved magnetograms, but using only He I dark points as proxies for the XBPs, indicated that the XBP are associated with cancelling flux (Martin and Harvey 1979; Martin et al. 1985; Harvey 1985). As an example of the magnetic evolution associated with XBPs, we show in Figure 2 the long range development of the magnetic bipoles associated with two of the XBPs from the December 11 data. We use the Kitt Peak magnetograms from December 10 (22 hours before launch), the preflight magnetogram (3 hours before launch), the postlight magnetogram (2 hours after launch), and the 12 December magnetogram (22 hours after launch). All of the magnetograms have been rotated to the time of flight in order to present them at the same solar geometrical position. The top example would appear to be associated with disappearing flux, and the middle example with emerging flux.

The temporal resolution of the daily full disk magnetogram observations from Kitt Peak is not adequate to conclusively classify the magnetic evolution of most of the observed XBP-associated BMRs. We do not have the magnetograph temporal coverage in the HRTS field of view to perform such an analysis at this location with the December 11 data. However, over a large field in the southwest of the disk, covering the area where the HRTS instrument had been planned to point, extensive coverage was maintained by the Big Bear videomagnetograph in order to perform just such an analysis. Webb and Moses

(1990) studied the x-ray and videomagnetogram data from both the August 15 and December 11 AS&E flights, and because of the excellent temporal coverage of the videomagnetograph data were able to characterize the magnetic bipoles corresponding to XBPs as emerging, stationary, or disappearing BMRs. They found that the most significant association was with disappearing flux regions.

We give in Table 2 an update of the results of Webb and Moses (1990) for the December 11 observations. We refer the reader back to the original paper for a fuller description of the analysis. The difference in the data presented in Table 2 is in a further refinement of the XBP identifications, and the presentation of the December 11 data alone instead of the combined August 15 and December 11 data. All XBP identifications have been reviewed, and classified as either certain or probable. In Table 2 the total number of XBPs and BMRs in the field are given, and the number of XBP associations with each type of BMR, for both the certain and the certain plus probable XBP identifications. This is compared with the expected result for a random surface distribution of XBPs, and with the staqndard deviation of the actual observed result from the expected result if the distribution of XBPs were random.

The results in Table 2 show that about 60% of the BMRs associated with XBPs were disappearing flux regions, around 5% were emerging flux regions, and around 25% were stationary flux regions. The stationary BMR identifications probably contain some fraction that would, with further study, show themselves to be disappearing, or even emerging, flux regions. It seems clear that the predominant association of XBPs in this area is with diappearing BMRs, or with cancelling magnetic flux. However, we note that only 10% of all identified BMRs were in fact associated with an XBP at all.

(ii) XBPs and He I Features

It is clear that a study of the evolution of the XBP magnetic structure requires a sequence of high resolution magnetograms and coronal images over many hours. Due to the temporal restrictions of sounding rocket flights, the only uninterrupted sequence of coronal x-ray images in existance is the Skylab observations, which were made before the development of the current generation of high temporal and spatial resolution magnetographs. A groundbased observation that could be used as a proxy for the x-ray coronal image would be extremely useful for this investigation. He I 10830 Å dark points have been widely used as such a proxy.

The solar He I lines observed at visible wavelengths are produced by transitions which arise from excited states greater than 20 eV above the atomic ground level. Goldberg (1939) showed that these excited neutral helium states could be populated by photoexcitation from UV radiation. Milkey, Heasley, and Beebe (1973) modeled this He I excitation using OSO-IV data to constrain the UV input, and found that the He I excitation mechanism was a combination of collisional excitation at the temperature and density of the high temperature regions of the chromosphere, and UV photoexcitation in the low temperature regions of the chromosphere. In this case, one would expect that He I images would show both the density structure of the high temperature chromosphere, and the structure of the UV emitting material, presumably transition region and coronal plasmas, overlying the low temperature chromospheric material. Zirin (1988) argued that the He I excitation in the Sun is exclusively from photoexcitation. However, the threshold for photoexcitation to higher energy levels of He I, below 504 Å, is at a much longer wavelength than the wavelengths at which 1.7×10^6 K coronal plasmas typical of XBPs, radiate most of their energy.

In He I 10830 Å images, small He I dark points have been found to be related to XBPs (Harvey et al. 1975). From this beginning, a number of studies

have been made to either refine this relationship, or (simply assuming that He I dark points are a proxy) to determine He I dark point properties and ascribe them to XBPs. Golub et al. (1989) give a recent analysis of He I dark points and references to earlier work.

We also have examined the correspondence of XBPs and the He I 10830 Å image for the December 11 data. Our first concern was simply to examine what was actually coincident in the He I image with the sites of XBPs. We find in the 11 December observations that it is almost always possible to identify a He I dark feature that is the clear counterpart of an XBP. These features are often not at all point-like, and independent identifications, clearly with a subjective basis, of dark points in a He I 10830 Å image and XBPs in an x-ray image, will sometimes result in XBPs without an identified He I dark point, and in identified dark points without a corresponding XBP. However, we find that a dark feature is almost always present, and often with a structure which is reminiscent of double ribbons. We often find two close points, two parallel elongated dark features, a "T" pattern, or a "V" pattern, in He I dark features corresponding to XBPs. Their structure is usually related to the orientation of the corresponding magnetic bipole on the magnetogram. In Figure 2 we show several examples of He I dark features, magnetogram bipoles, and XBPs. The top example shows a He I double ribbon feature, and the middle example a quite complex He I dark feature with several structurally elongated elements. These suggest the ribbons connected with arcades of loops often seen at much greater scale in solar flares. In the bottom example we see a He I dark feature which is a pair of dark points, with a corresponding XBP. However a similar pair at the bottom of the area shown has no XBP counterpart; its corresponding location on the x-ray image is marked by an arrow. We suggest that it is significant that these He I dark features seem morphologically similar to the ribbons showing locations of loop footpoints in the chromosphere and transition region,

and not the loops spanning ribbons in coronal plasmas. This ribbon structure may be a consequence of the emission from transition region temperature plasmas which are emitted at wavelengths shortward of 504 Å, such as the helium continua, and are actually stronger than the coronal emissions in this range.

We have also examined the usefulness of the traditional He I dark points as a proxy for XBPs by studying the statistical correlation of He I dark points and XBPs, using the data from both the August 15 and December 11 sounding rocket flights. A map of XBP identifications was made as described in the previous discussion on coalignment of data. An independent map of He I dark point identifications was made as in previous work by Harvey (1985). The maps were restricted to definite XBPs, and to unobscured He I dark points, both within 60° of Sun center to avoid extreme line of sight effects and center to limb variation. The results of this comparison are presented in Table 3. We note that similar results were obtained by Golub et al. (1989) using data from previous AS&E rocket flights.

As seen from Table 3, more XBPs than He I dark points (DPs) were identified in this exercise. This is in part a consequence of the different ways the minimum thresholds for identification of XBPs and He I DPs were determined. The threshold for XBP identification was set by the limit for instrumental detection. The number of XBPs detected increases with exposure time for the shorter exposures, but levels off asymptotically for the longer exposures (Golub et al. 1974). In the 60 s exposure which was used to identify XBPs with the December 11 data, esentially all XBP present on the Sun should be detected. The threshold for He I DP identification was first set by predetermined requirements on candidate size, contrast, and darkness which were actually well above the limit of instrumental detection. An attempt was made to extend the number of candidates by lowering the threshold for DP identification. The result of this extension was that the fraction of XBPs with DP associations increased to

approach 100%, while the fraction of He I DPs without XBP associations also increased greatly. As the threshold for DP identification is lowered, many more features are included in the study which do not have an XBP counterpart.

Further work on the use of He I DPs as an XBP proxy is in progress. J. Harvey is refining the use of an automated computer DP selection program to reduce the subjective aspect of DP selection. This program acts as a filter for DP candidates. Much more effort is required to implement a similar program for XBP selection, since the x-ray background of the XBPs varies greatly over the disk. Additional information is still required to separate compact He I features with coronal associations from those of only chromospheric network origin. Since the XBP correlation with magnetic bipoles is strong, this can be used to separate He I candidate features with possible XBP assosciations. The He I DP program will then function as the product of two filters: one based on morphological properties of candidates in the He I image, and the second based on properties of photospheric magnetograms, which might include the temporal evolution of the magnetic field. It may also be necessary to include another filter based on chromospheric information if the excitation of He I includes a significant collisional component. However, the possibility of groundbased continuous detection of XBPs using a reliable proxy, for studies of the solar cycle evolution of small scale coronal structures, is exciting.

VI. TRANSITION REGION EXPLOSIVE EVENTS

Explosive events are small spatial scale, wide profile, transient features observed in transition region temperature plasmas throughout the quiet Sun (see review by Cook 1990). They are best seen in the strong C IV 1548 Å and 1550 Å lines, but can also be observed in lines covering a temperature range from 20,000 K (Lα, C II) to 250,000 K (O V). Explosive events have broadened profiles of order 100 km s^{-1} to the blue, to the red, or both. They are

interesting as a possible signature of the occurrence of microflares in the quiet solar atmosphere, which have been proposed as the heating mechanism of the corona and transition region. A microflare would be a small spatial scale, rapid release of energy driven by some form of magnetic reconnection, and manifested observationally by transient brightening, Doppler motions, or plasma turbulence, as seen in more dramatic form in full scale solar flares.

The first analysis of these events, from HRTS I and HRTS II observations, was performed by Brueckner and Bartoe (1983; see also Dere, Bartoe, and Brueckner 1989 for a later analysis of HRTS III data on these events), who estimated the mass and kinetic energy fluxes contained in explosive events. We can see now that their answer, that these events can directly supply the mechanical energy to heat the transition region and corona through dissipation of their kinetic energy, was too extreme. This is because the value used for the average event velocity, 400 km s^{-1}, was too large, and the kinetic energy flux goes as the cube of velocity. As became clearer after examining more data, the HRTS II C IV explosive events are the most dramatic and energetic yet observed, and not typical.

It was not until the Spacelab 2 flight in July - August 1985 (see Brueckner et al. 1986, Dere et al. 1987 for general reviews of the HRTS experiment on Spacelab 2) that a large database became available to study the statistics of these events. A survey program sampled approximately 25% of the disk in 13 individual raster sequences over four consecutive orbits of the space shuttle. An analysis of these observations was given by Cook et al. (1987). They found an average leading edge velocity of the line profiles of 80 km s^{-1} (in this data set the highest velocity encountered was 200 km s^{-1}), an average size of 2 arc sec, and an average lifetime of no greater than 90 s. Using these parameters, Cook et al. found that the explosive events did not directly represent enough available energy when dissipated to heat the corona or transition region in

situ. However, they suggested that the explosive events are the byproducts of extremely turbulent energy dissipation from a nonthermal primary heating event, which presumably could be magnetic reconnection in a microflare. Thus the relationship of explosive events with x-ray emission, showing if heating to coronal temperatures is occuring, and the relationship with the magnetic field (network, bipoles), are important to determine.

(i) XBPs and C IV Explosive Events

The correspondence between coronal XBPs and transition region explosive events was examined using the coaligned x-ray image and map of sites of C IV explosive events, shown in Figure 6. Within the field of the HRTS raster, 505 explosive events were identified and 12 XBPs were identified. The number of explosive event locations (11) that overlapped an area of XBP emission (as recorded in the deepest x-ray exposure) was comparable to the number of overlapping locations (12.5) expected from random and independent distributions within the HRTS raster area of explosive events and XBPs. Only 5 of the 12 XBPs within the raster area had any coincident explosive event locations.

The XBPs are clearly not the coronal extensions of the transition region explosive events. In our observations, the presence of an explosive event is not necessarily accompanied by the presence of an XBP and the presence of an XBP is not necessarily accompanied by the presence of an explosive event. However, these observations do not preclude an interaction between XBPs and explosive events which requires a time series of observations to determine. For example, it is interesting that the brightest and most compact XBP is associated with the largest number of explosive events (4 events).

(ii) Explosive Events and the Supergranular Network

We have compared the location of sites of explosive events, using our C IV map, with the coaligned magnetogram, He I 10830 Å image, and 1600 Å spectroheliograph image, in order to look for the relationship of C IV explosive events to the supergranular network. We found that the explosive events appear to be located at the edges of strong field network elements, or even within network elements of weakest magnetic field. In Figure 3 the HRTS C IV map and 1600 Å image are shown aligned with the x-ray, magnetograph, and He I 10830 Å images over our complete field of view. To illustrate our conclusion we show in Figure 4 an enlargement of a section of the C IV explosive event map superposed on the HRTS 1600 Å spectroheliograph and the He I 10830 Å images, which show the location of the network. We see that the explosive events appear to be concentrated at the edges of strong network, or sometimes within weaker network areas, in this quiet area; they appear to generally avoid areas completely away from network such as cell centers.

(iii) XBPs and C IV Counterparts

We also determined the transition region spectral features which did correspond with the sites of coronal XBPs. These were found to be larger, brighter structures in C IV than the high velocity explosive events, sometimes with a complex, sheared velocity structure apparent in the line profile, but which, however, never reached the ~100 km s^{-1} velocities seen in the C IV events. Figure 5 shows the HRTS C IV feature corresponding to the prominent XBP at the right side of the raster pattern, toward Sun center, the brightest example in the HRTS field. Two consecutive raster steps are illustrated. The XBP, which covers a total raster width in the complete series of raster steps which is approximately equal to its length along the slit, is seen in both raster steps. A prominent C IV energetic event is also seen in one raster step, but is not present on the step just 2 arc sec away. We also see another C IV

spectral feature, seemingly no different than that corresponding to the XBP, which does not have an XBP counterpart.

As discussed in § V(i), the XBPs are associated with obvious magnetic bipoles in the magnetogram, and occur at the sites of network elements which correspond to the magnetic BMRs. Network elements are composed of patches of strong magnetic field concentrated by the supergranular flow, and at the T_{min} level network elements corresponding to magnetic BMRs are no brighter than network elements corresponding to unipolar magnetic fields of similar total absolute magnetic flux. But only those network elements corresponding to BMRs can be the site of an XBP. The second C IV network feature in Figure 5 which had no XBP counterpart corresponds to a unipolar region in the magnetogram.

We can make a continuity argument to relate the ~20 km s^{-1} velocity signature observed in the C IV brightenings associated with XBPs earlier, to the velocities inferred by others for the coronal and chromospheric components of XBPs. Achmad and Webb (1978) inferred a >100 km s^{-1} outward velocity in polar plumes associated with XBPs, which compares favorably with the tenfold decrease in density of the corona relative to the transition region. Holt and Mullan (1986) reported a 2 km s^{-1} blueshifted component in Ca II K observations at the locations of He I dark points in coronal holes. If these dark points can be taken as proxies for XBPs, then the magnitude of this velocity compare favorably to the tenfold increase in density of the chromosphere relative to the transition region. The observation that the C IV brightenings and the He I dark points are of the same spatial scale as the XBP forms the basis of this comparison. However, we note that most of the Doppler shifts in the transition region material are to the redward of the line center. This continuity argument should only be taken as a suggestion for future simultaneous observations, and not as an independent result of the XBP campaign.

(iv) X-ray Dark Lanes and C IV Explosive Events

The x-ray image seen in Figure 1 shows, besides both bright active regions and bright, compact XBPs in quiet areas, in addition several types of region of low x-ray intensity. These include coronal holes, both at the limb and also a low-latitude coronal hole on the southeast disk, and filament channels, such as the example in the northeast disk above the HRTS field of view. In addition, however, we can also identify in quiet regions narrow, winding, elongated areas of low intensity which we call dark lanes. These are distinct from either filament channels or coronal holes. Filament channels are dark areas in x-rays which correspond to sites where filaments are observed in such cooler lines as Hα, Ca II K, or He I 10830 Å, and correspond to neutral lines in a magnetogram. The quiet Sun coronal dark lanes do not contain filaments, and did not contain filaments on the previous or following day's He I 10830 Å images. Coronal holes occur in regions of unipolar field, such as polar regions, or occassionally disk areas at lower latitudes. Kitt Peak magnetograms have a noise level near 7 G, and in the approximate range 7 - 30 G one can find a weak, mixed polarity field in quiet areas almost anywhere on the disk. But in unipolar regions there is an additional stronger field component which is predominantly of one polarity. On December 11 a low-latitude coronal hole was present in the southeast in such a unipolar region. We will see that dark lanes, however, actually correspond on the magnetogram to weak field, mixed polarity regions.

In Figure 6 we show a section of the x-ray image with the C IV explosive event map superposed. The x-ray image shows a dark lanes within the HRTS field, and the C IV events appear to be predominantly concentrated within this dark lane, avoiding areas of hazy, brighter x-ray emission probably corresponding to weak, unresolved loop systems in quiet areas of the disk.

Attention is drawn to the coronal dark lanes only from the comparison with the HRTS C IV explosive events map. Dark lane structure can be recognized on

previous x-ray images, although the dark lanes may be observed here more easily in the long exposure December 11 image because of the pointing stabililty of the sounding rocket attitude control system, the improvement in image contrast and relatively lower scattering with the cleaned, fused silica mirror. But until the connection with C IV explosive events, there was no particular reason for interest in dark lanes.

We have formed a contour around around the x-ray dark lane using our image processing system, by enhancing low intensities, smoothing the image slightly, and reducing the number of intensity levels to further simplify the image. Our resulting contour can be seen in Figure 7, superposed on the Kitt Peak magnetogram and He I 10839 Å images and a HRTS 1600 Å spectroheliogram. This contour does not accurately trace the x-ray dark lane approaching the limb because of line of sight effects. In the x-ray image the dark lane can still be seen as a morphological feature toward the limb, and a large number of C IV explosive events occur in this area, but the changing contrast toward the limb in the x-ray image makes it impossible to trace the complete outline with only one contour level. However, for comparison with the magnetogram and He I 10830 Å images this is not a drawback, since they also are affected by center-to-limb changes, and comparisons are best made in the more disk center area of the HRTS field of view.

We see that the dark lane is associated with a weak, mixed polarity area in the magnetogram, and with areas of network weakening in the He I 10830 Å image, although to a less obvious extent than the network weakening of the disk coronal hole area, which forms a larger, more contiguous, unified area. (In Figure 7, only the lowest area of the large, bottom contour corresponds to the coronal hole; compare the full disk x-ray image of Figure 1, the magnetogram of Figure 7 where it shows strong, unipolar positive polarity field, and the He I 10830 Å and x-ray images of Figure 7.) In both the magnetogram and the He I 10830 Å

image the contour snakes around or excludes strong field areas and bipoles, and He I strong network and He I dark points. The dark lane area would not be obvious in these images beforehand because of the local intrusions of stronger areas. It is possible that the dark lanes may be viewed as the weakest level of the coronal hole phenomenum, although an unambiguous unipolar magnetic field is not present.

We find that the number of C IV explosive events per unit area within the dark lane is approximately twice the value outside the dark lane, and in addition that its numerical value is greater than we would have expected from the results of a disk survey undertaken on the Spacelab 2 flight of the HRTS payload (Cook et al. 1987). The Spacelab 2 number density, 4000 events at any time on the full surface area, corresponds to 3.5×10^{-4} events per arc sec^2. We found from this analysis approximately 2.3×10^{-3} events per arc sec^2 outside dark lanes, and 4.6×10^{-3} events per arc sec^2 inside the dark lane. This is possibly because of the occurence of a particularly rich region in the field of view, associated with the x-ray dark lane, while the Spacelab 2 result was from a survey covering 25% of the flat disk, and by an extended detection threshhold from better spatial resolution with the HRTS V data. The difficulty in sampling to the same detection threshhold in different observations means that these numbers, especially when making comparisons between different observations, must not be pushed too far. But it appears that the number of smaller, weaker events in the full range of explosive events may be greater than estimated from the Spacelab 2 results.

VII. DISCUSSION

An original goal of the bright point campaign was to determine the correspondence of transition region explosive events seen in C IV with photospheric magnetograms and with coronal XBPs. We found that these events

appear to be concentrated at the edges of strong network, or in weaker network regions, in the quiet Sun, and are not simply the transition region counterparts of XBPs. The x-ray image shows a pattern of dark lanes in quiet Sun areas, and the C IV events appear to be predominantly concentrated within these dark lanes, avoiding areas of hazy, slightly brighter x-ray emission probably corresponding to unresolved loop systems seen even in quiet region areas of the disk.

It is highly suggestive that the explosive events are associated with the edges of network elements. Magnetic fields within cell centers are swept by the supergranular flow to the cell boundaries, and somehow concentrated into the strong field network elements. We can speculate that the explosive events arise from reconnection of relatively small scale flux elements from the cell centers when they encounter an opposite polarity strong field network element. We note again that Webb and Moses (1990) found that XBPs are associated with disappearing magnetic bipoles more often than with either emerging or stationary bipoles, and it is qualitatively plausible to think of the disappearance of flux as the sign of magnetic reconnection. In fact, there is possibly an indirect connection with spicules, which also may be related to this sweeping of fields to the cell boundary network elements. However their observational properties of size, lifetime, and total number are very different. The explosive events seem to have overpowered the local magnetic field, while spicules seem more a dynamical, longer lived response to localized heating, still contained by the magnetic field topology.

We have been unable to determine if the individual C IV events are associated with magnetic BMRs, as are the XBPs, although it is clear that such an association if it exists must be with much weaker bipoles than those associated with XBPs. In examing magnetograms which are displayed to bring up the weaker field regions (7-30 G), mixed polarity small scale features appear everywhere in the quiet Sun. The Kitt Peak magnetograph data is from many hours

before the rocket flight. We would need to obtain a time sequence of more truly simultaneous data, and more importantly develop an objective criterion to claim an association with a unique bipole out of all those present, to determine the answer.

The XBPs are associated with magnetic bipoles in the magnetograms, with dark features in the He I 10830 Å data, with bright network elements in HRTS 1600 Å spectroheliograms, and with 10-20 arc sec bright network emission with complex sheared velocity fields in the HRTS C IV spectra. However none of these associations is unique; in each case similar features exist which do not have an XBP counterpart. A major goal of future observations must be to determine what factor accounts for the continued heating of some small loop systems to coronal temperatures, resulting in an XBP, while other apparently similar structures are not so heated. We can speculate, from the association of XBPs with disappearing flux, that snapshot observations will not differentiate these two types of loop systems, but that temporal coverage of the earliest phases of development of an XBP may show some differentiator, such as a characteristic onset of disappearing magnetic flux.

The bright point campaign provides an example for the type of collaborative programs which might be attempted during the solar maximum period 1990-1991. Although there were certainly logistical problems in coordinating multiple sounding rocket launches and simultaneous groundbased observations, the scientific return was more than correspondingly greater. Further, simultaneous observations from all levels of the solar atmosphere are clearly an essential tool for obtaining new insight into solar phenomena and must form the basis of any space mission such as the Orbiting Solar Laboratory.

This work was supported by NASA under DPR W-14,541 (J.-D.F Bartoe, G.E. Brueckner, J.W. Cook, and K.P. Dere), NAS5-25496 (D. Moses), and NAS5-31619 (D. Moses), and by the Office of Naval Research. During the preparation, launch, and initial data analysis of the AS&E sounding rocket program, D. Moses was affiliated with AS&E.

TABLE 1

COLLABORATIVE OBSERVATIONS

Day of 1987	Time (UT)		Observation
December 10	20:46		Kitt Peak magnetogram
	21:40		Kitt Peak He I
December 11	15:03		Kitt Peak magnetogram
	15:30-	*	Big Bear videomagnetograms
	19:00		(southwestern area)
	17:00-	*	Kitt Peak He I (19 area
	18:51		scans in southwest area)
	18:15		AS&E sounding rocket launched
	18:45	*	NRL sounding rocket launched
	19:15		Kitt Peak He I
	20:37		Kitt Peak magnetogram
December 12	16:08		Kitt Peak magnetogram
	17:06		Kitt Peak He I

All data full disk except those marked *

TABLE 2

CORRESPONDENCE OF XBPs AND BIPOLAR MAGNETIC FEATURES (BMFs)

WITHIN 1987 DECEMBER 11 VIDEOMAGNETOGRAPH FIELD

Feature	Total No. Observed	Associated With XBP	Fraction Counterpart	Expected XBP Association	Standard Deviation
XBP	20 (24)				
Cancelling BMR	60	12.5 (14.5)	63% (60%)	5.8	2.8 (3.6)
Emerging BMR	25	1 (1.5)	5% (6%)	2.4	<1 (1.5)
Stationary BMR	163	5.5 (5.5)	28% (23%)	15.8	2.6 ( )
Total BMRs	248				
No BMR found		1 (2.5)	5% (10%)	0	

*XBP identifications are classed as certain or as probable. Results from the certain identifications are unmarked, while results from combined certain and probable XBP identifications are enclosed in parentheses. Fractional attribution occured when an XBP could be plausably associated with two close BMRs of differing classification.

TABLE 3

CORRESPONDENCE OF XBPs AND He I 10830 Å DARK POINTS

WITHIN 60° OF SUN CENTER

Date 1987	Total No. XBPs	Total No. He I DPs	No. of Paired Counterparts	Fraction Counterpart: XBPs	He I DPs
August 15	105	46	24	23%	52%
December 11	32	30	14	44%	47%
Combined	137	76	38	28%	50%

REFERENCES

Ahmad, I.A., and Webb, D.F. 1978, Solar Phys., 58, 323.

Brueckner, G.E., and Bartoe, J.-D.F. 1983, Ap. J., 272, 329.

Brueckner, G.E., Bartoe, J.-D.F., Cook, J.W., Dere, K.P., and Socker, D.G. 1986, Adv. Space Res., 6, 263.

Cook, J.W. 1990, in Mechanisms of Chromospheric and Coronal Heating, ed. P. Ulmschneider, E. Priest, and R. Rosner (Berlin: Springer), in press.

Cook, J.W., and Brueckner, G.E. 1991, in The Solar Interior and Atmosphere, ed. A.N. Cox, W.C. Livingston, and M.S. Matthews (Tucson: University of Arizona Press), in press.

Cook, J.W., Brueckner, G.E., and Bartoe, J.-D.F. 1983, Ap. J. Lett., 270, L89.

Cook, J.W., and Ewing, J.A. 1990, Ap. J., 355, 719.

Cook, J.W., Lund, P.A., Bartoe, J.-D.F., Brueckner, G.E., Dere. K.P., and Socker,G.D., 1987, Fifth Cambridge Workshop on Cool Stars, Stellar Systems, and the Sun, ed. J.L. Linsky and R.E. Stencel (New York: Springer), 150.

Dere, K.P., Bartoe, J.-D.F., and Brueckner, G.E. 1989, Solar Phys., 123, 41.

Dere, K.P., Bartoe, J.-D.F., Brueckner, G.E., Cook, J.W., and Socker, D.G. 1987, Science, 238, 1267.

Goldberg, L. 1939, Ap. J., 89, 673.

Golub, L. 1980, Phil. Trans. Roy. Soc. Lond., 297, 595.

Golub, L., Harvey, K.L., Herant, M., and Webb, D.F. 1989, Solar Phys., 124, 211.

Golub, L., Herant, M., Kalata, K., Lovas, I., Nystrom, G., Pardo, F., Spiller, E., and Wilczynski, J. 1990, Nature, 344, 842.

Golub, L., Krieger, A.S., Harvey, J.W., and Vaiana, G.S. 1977, Solar Phys., 53, 111.

Golub, L., Krieger, A.S., Silk, J.K., Timothy, A.F., and Vaiana, G.S. 1974, Ap. J. Lett. 189, L93.

Golub, L., Krieger, A.S., and Vaiana, G.S. 1976, Solar Phys., 50, 311.

Haggerty, R., Simon, R., Golub, L., Silk, J.K., Timothy, A.F., and Vaiana, G.S. 1975, AAS Photo-Bulletin, 10, 8.

Harvey, J.L., Krieger, A.S., Timothy, A.F., and Vaiana, G.S. 1975, Osserv. Mem. Oss. Acertri, 104, 50.

Harvey, K.L. 1985, Austral. J. Phys., 38, 875.

Holt, R.D., and Mullan, D.J. 1986, Solar Phys., 107, 63.

Kjeldseth Moe, O., VanHoosier, M.E., Bartoe, J.-D.F., and Brueckner, G.E. 1976, A Spectral Atlas of the Sun Between 1175 and 2100 Angstroms, NRL Report 8056.

Krieger, A.S., Vaiana, G.S., and Van Speybroeck, L.P. 1971, in Solar Magnetic Fields (IAU Symposium No. 43), ed. R. Howard (Dordrecht: D. Reidel), p. 397.

Martin, S.F., and Harvey, K.L. 1979, Solar Phys., 64, 93.

Martin, S.F., Livi, S.H.B., Wang, J., and Shi, Z. 1985, in Measurements of Solar Vector Magnetic Fields (NASA Conference Publication 2374), ed. M.J. Hagyard (Wahington, DC: NASA), p. 403.

Milkey, R.W., Heasley, J.N., and Beebe, H.A. 1973, Ap. J., 186, 1043.

Moses, D., Schueller, R., Waljeski, K., and Davis, J.M. 1989, SPIE, 1159, .

Porter, J., Moore, R.L., Reichmann, E.J., Engvold, O., and Harvey, K.L. 1987, Ap. J., 323, 380.

Sheeley, N.R., Jr., and Golub, L. 1979, Solar Phys., 63, 119.

Vaiana, G.S., Krieger, A.S., and Timothy, A.F. 1973, Solar Phys., 32, 81.

Vernazza, J.E., Avrett, E.H., and Loeser, R. 1976, Ap J. Suppl., 30, 1.

Vernazza, J.E., Avrett, E.H., and Loeser, R. 1981, Ap J. Suppl., 45, 635.

Webb, D.F., and Moses, J.D. 1990, Adv. Space Res., 10, 185.

FIGURE CAPTIONS

Figure 1. Full disk soft x-ray photographic images used in the collaborative analysis. Top: 1987 August 15 image, 30 s exposure with polypropylene filter. Bottom: 1987 December 11 image, 60 s exposure with polypropylene filter.

Figure 2. Comparison of XBPs with Kitt Peak magnetograms and He I 10830 Å images. Top: 10 December magnetogram, 11 December preflight magnetogram, XBP and He I corresponding dark point, 11 December postflight magnetogram, 12 December magnetogram. Middle: Same comparison for a second XBP. Bottom: comparison of Kitt Peak He I 10830 Å dark points with x-ray image. The top He I dark point feature corresponds to an XBP, but the bottom similar He I dark point feature has no XBP counterpart.

Figure 3. The section of the solar disk containing the HRTS field. North at top, east at left. The map of sites of C IV explosive events is superposed on a HRTS 1600 Å spectroheliogram (top left), the AS&E x-ray image (bottom left), the Kitt Peak He I 10830 Å image (top right), and the Kitt Peak magnetogram (bottom right)

Figure 4. A section of the HRTS C IV explosive events map superposed on the He I 10830 Å image (top) and a HRTS 1600 Å spectroheliogram (bottom), illustrating the association of explosive events with network.

Figure 5. HRTS slit spectra of C IV 1548 Å and 1550 Å from two consecutive steps (24 and 25) of the third HRTS raster. The steps are 2 arc sec apart. The C IV counterpart to an XBP is shown, together with a C IV energetic event visible only in step 25.

Figure 6. The x-ray image, enhanced to bring out the dark lane, with the C IV explosive event map supperposed.

Figure 7. Comparison of the spatial area of the x-ray dark lane region and other dark x-ray regions, defined by a brightness contour level which selects them, with other images: the x-ray image with the dark lane, filament channel, and disk coronal hole areas (top left), the magnetogram with contour from the x-ray image superposed (top right), the He I 10830 Å image with contour superposed (lower left), and a HRTS 1600 Å spectroheliogram with contour superposed (lower right).

POSTAL ADDRESSES

John-David F. Bartoe Code 4162

Gunter E. Brueckner Code 4160

John W. Cook Code 4163

Kenneth P. Dere Code 4163

Naval Research Laboratory

Washington, DC 20375-5000

Dan Moses

Bendix Field Engineering Corp.

6178 Oxon Hill Road

Oxon Hill, MD 20745

John M. Davis

Marshall Space Flight Center

Huntsville, AL 35812

John W. Harvey

Frank Recely

National Solar Observatory

Tucson, AZ 85721

Sara F. Martin

Harold Zirin

Big Bear Solar Observatory

California Institute of Technology

Pasadena, CA 91125

David Webb

Emmanuel College

Boston, MA 02115

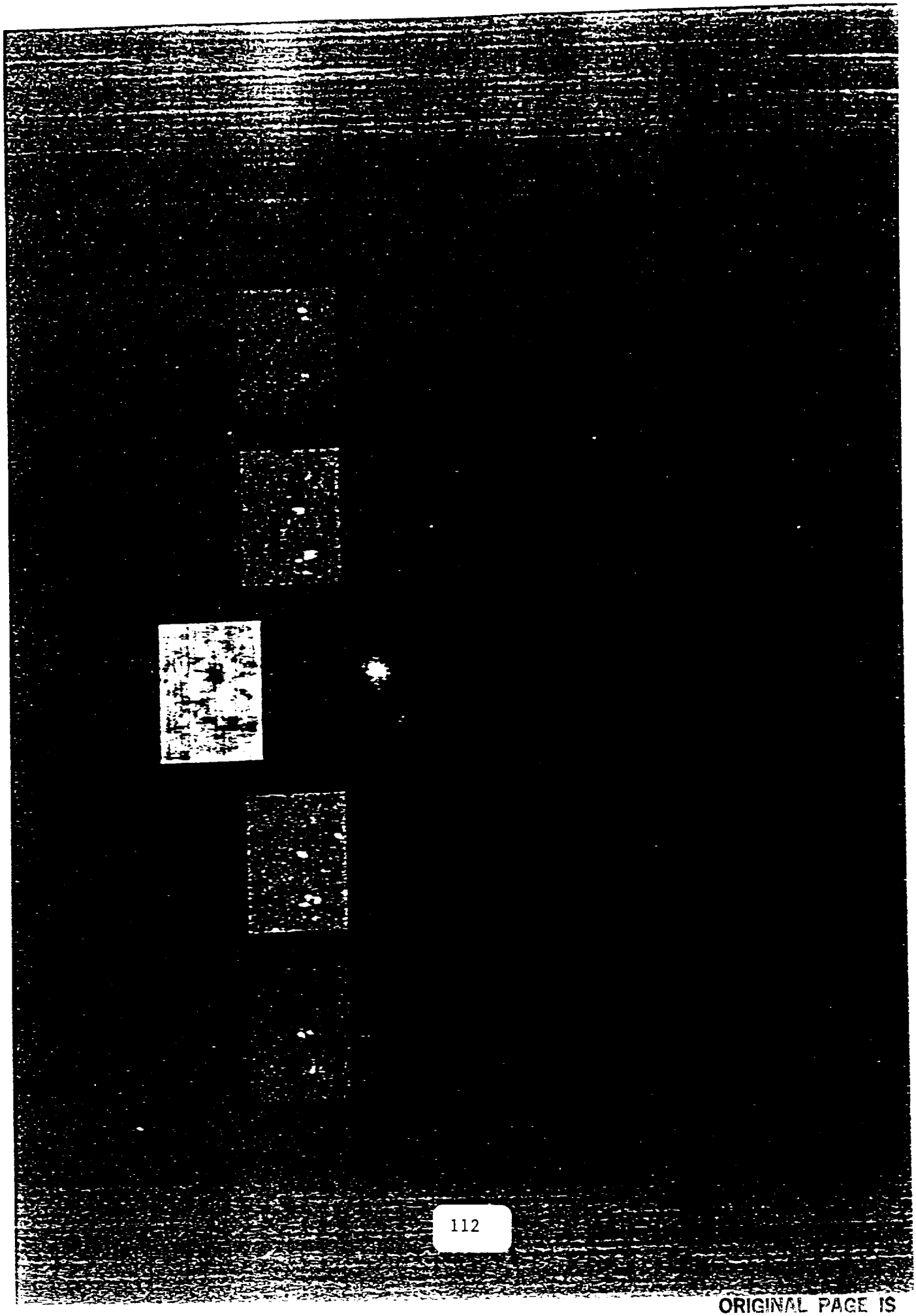

Fig 2 (top)

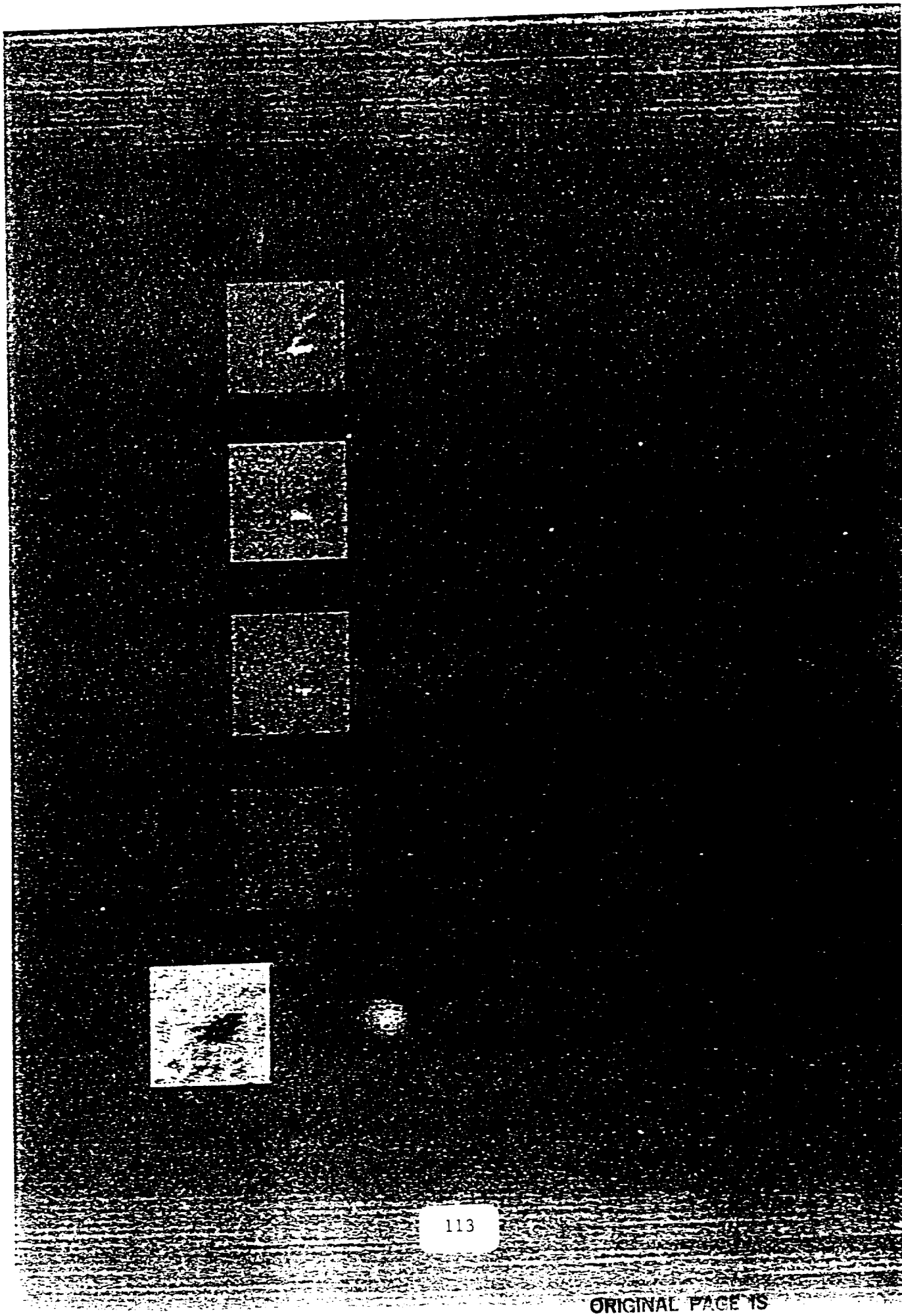

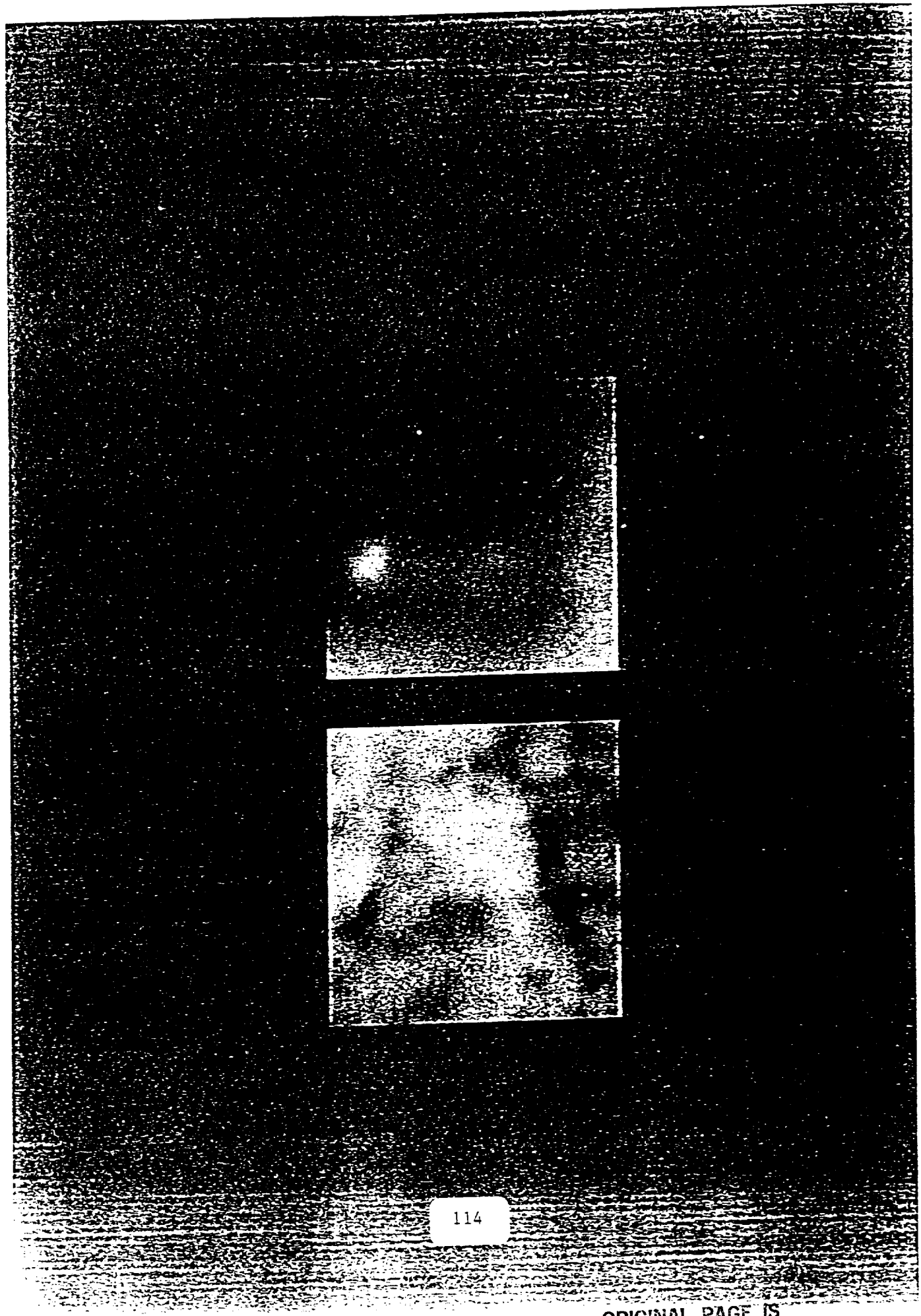

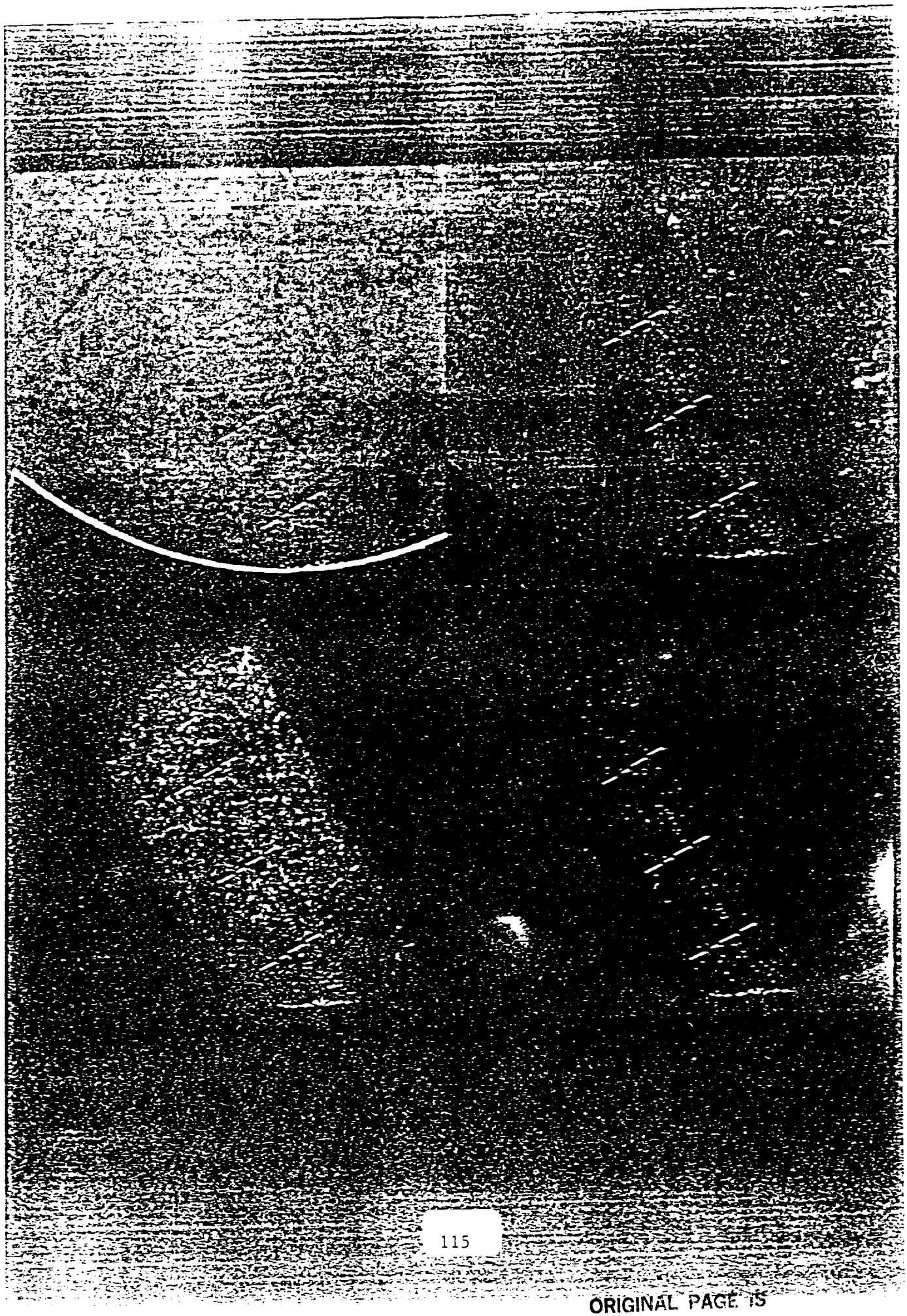

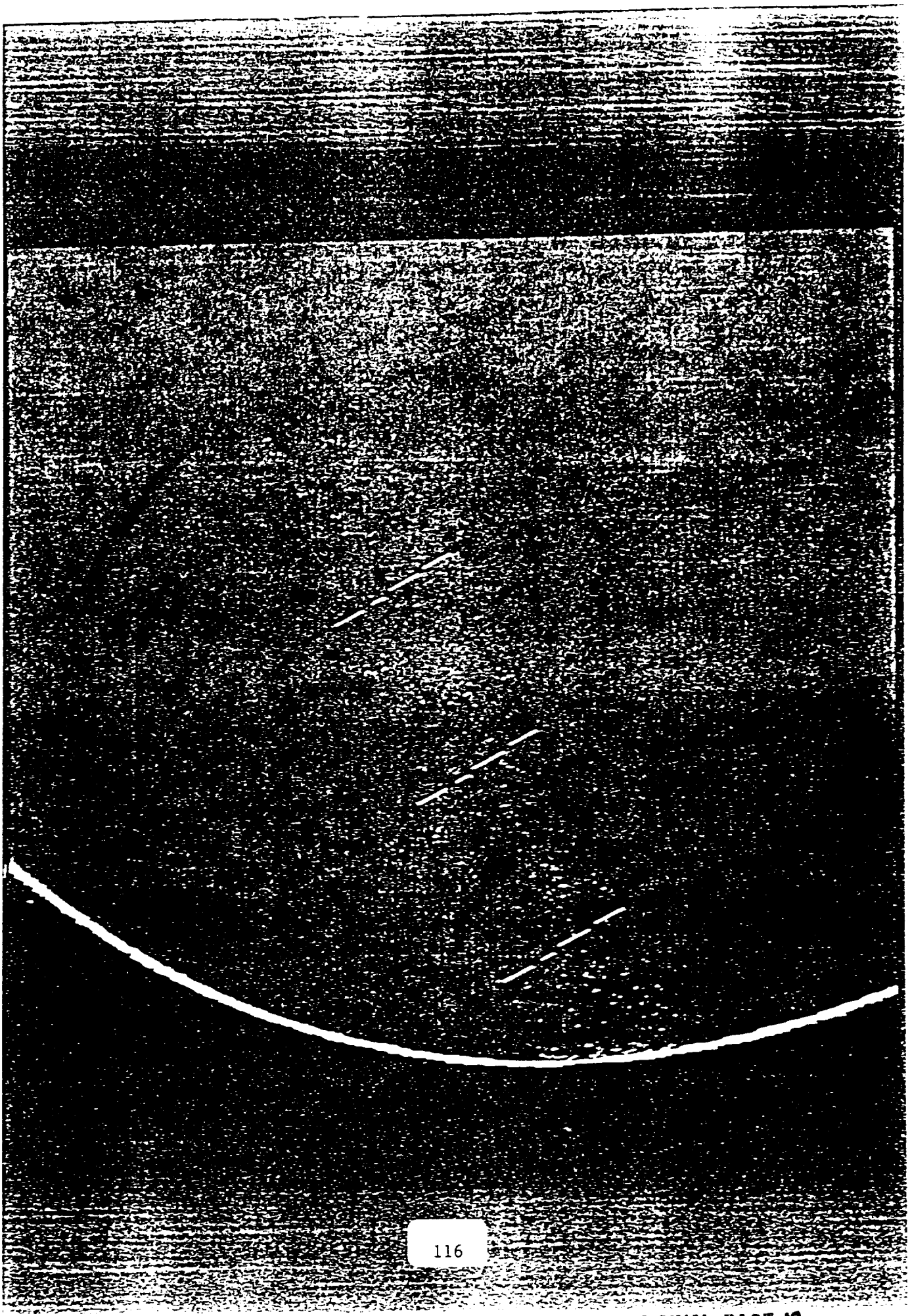

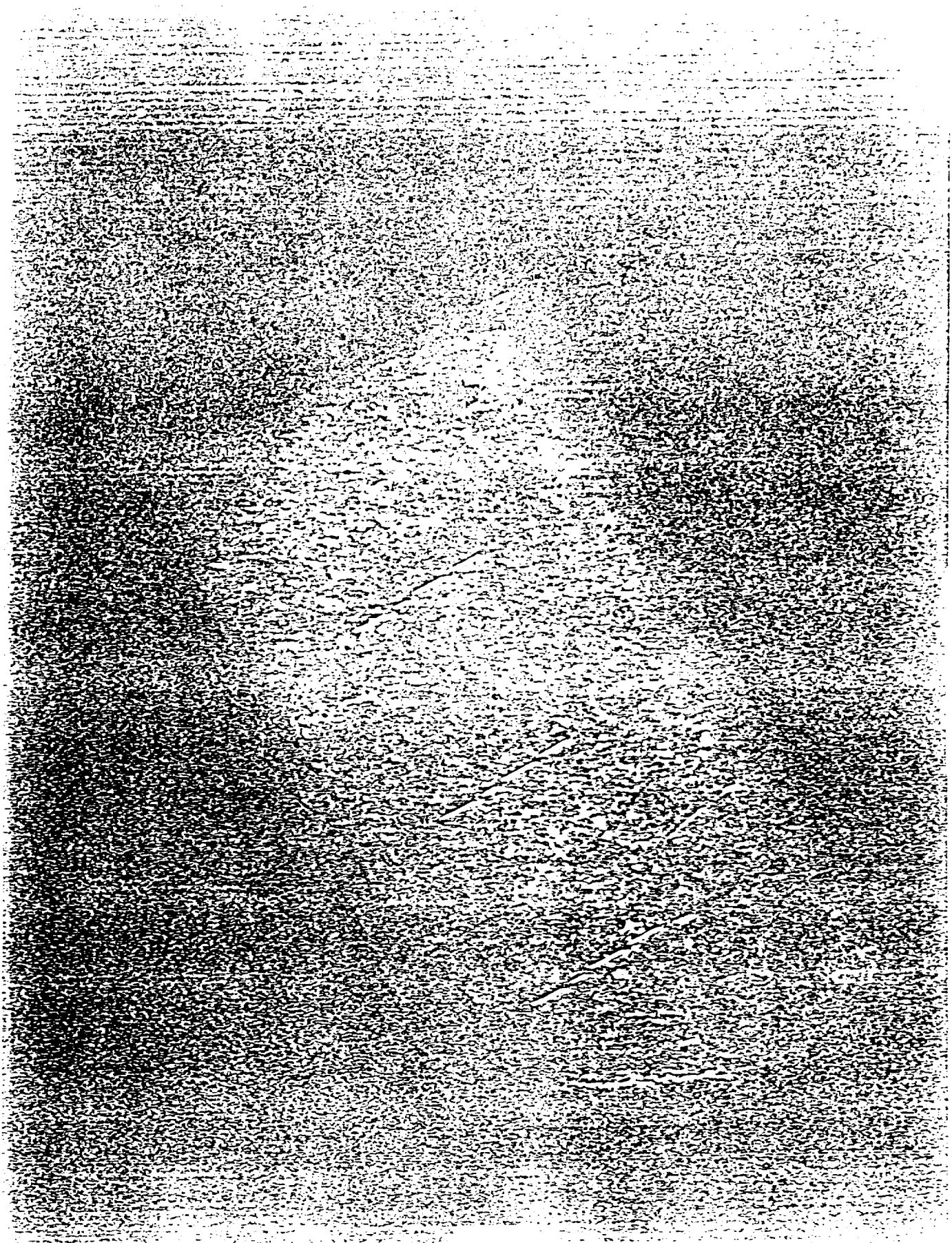

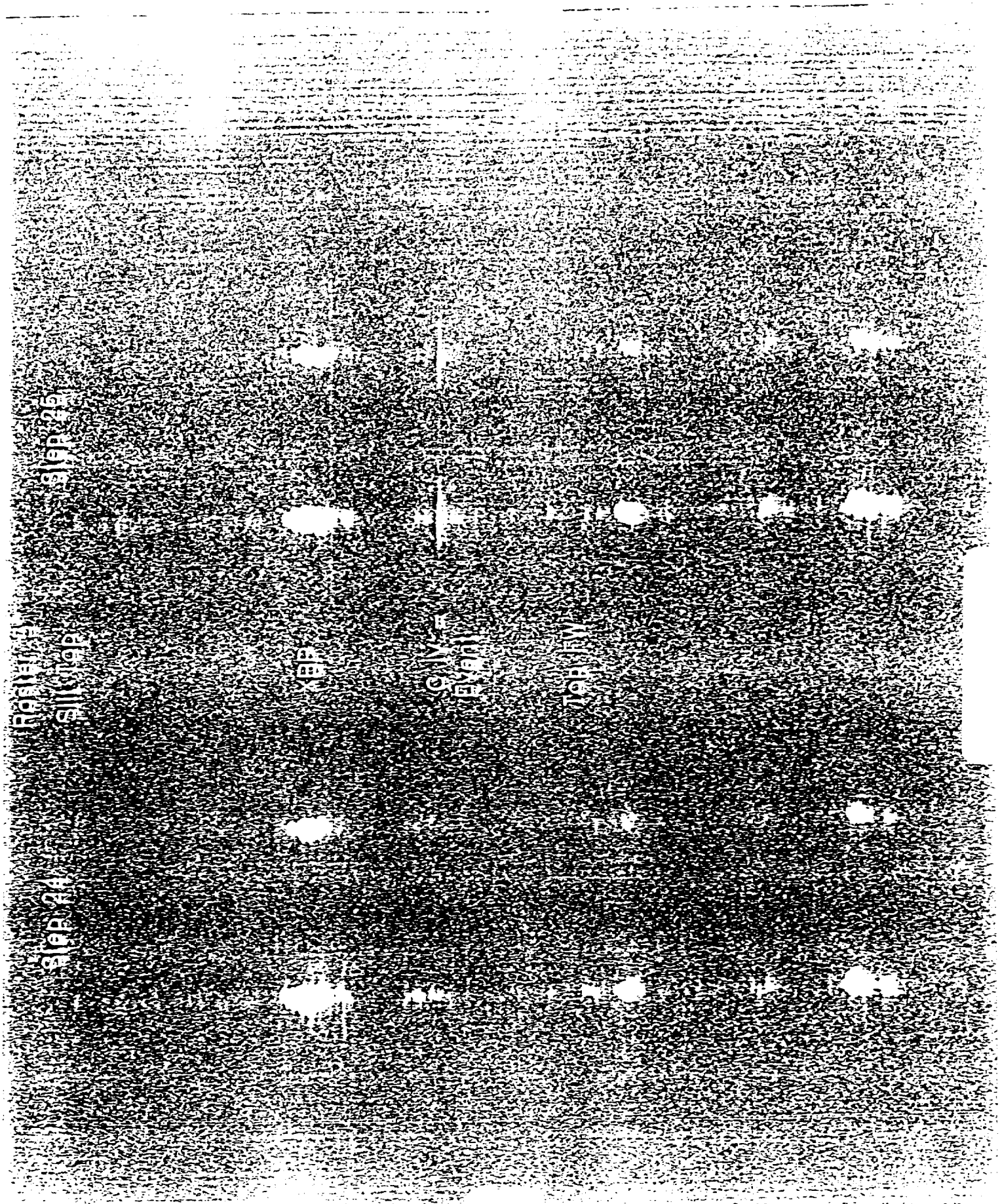

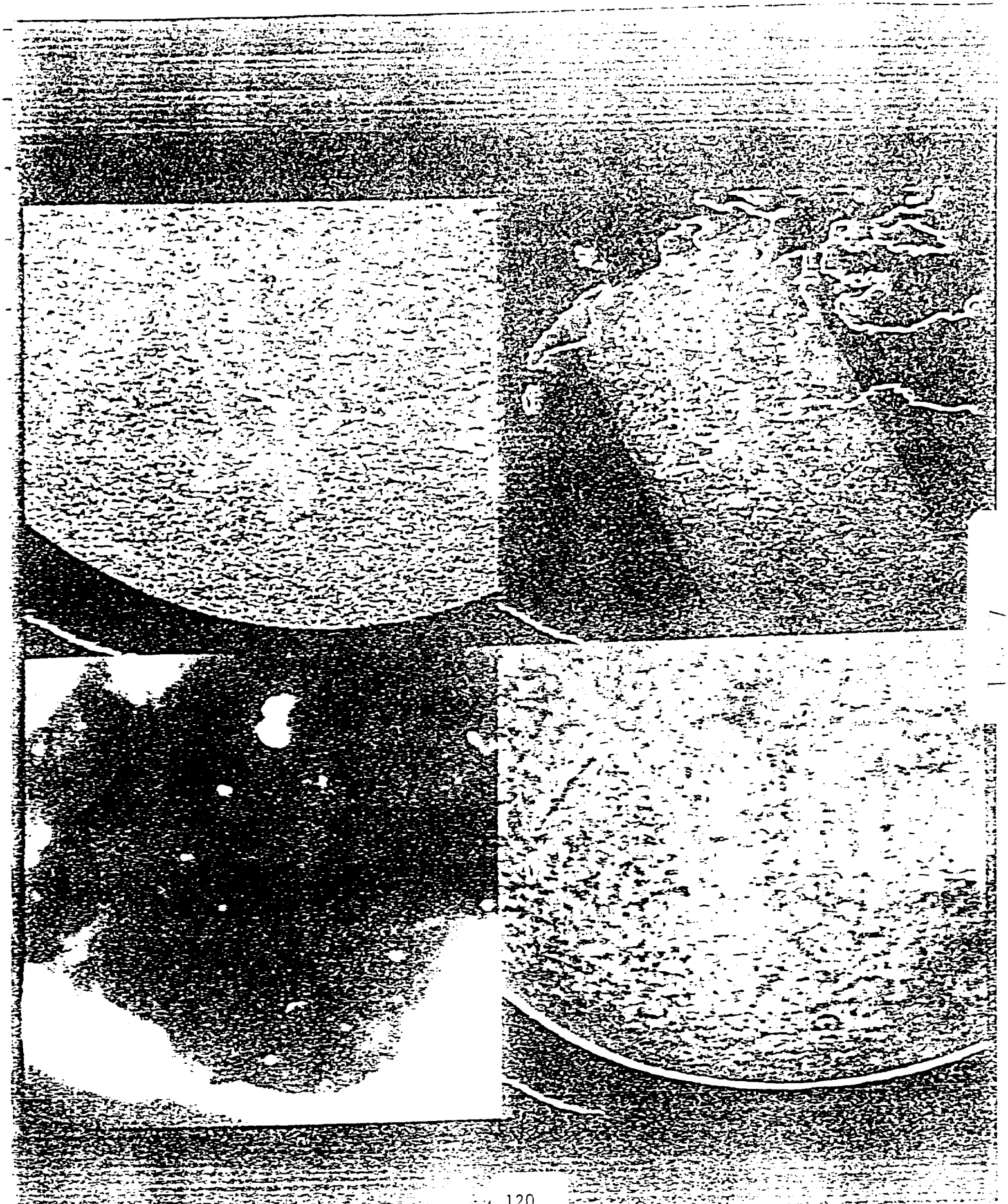

APPENDIX E: LIST OF DRAWINGS AVAILABLE FOR THE CURRENT AND EARLIER PAYLOADS

Size	Drawing No.	Description	Subsystem
		MECHANICAL DRAWINGS	
E	100108-A	Grazing incidence mirror	Optical
E	100109-A	Mirror Assembly	Optical
E	100133	Split Retention Ring	Optical
C	100137-2	X-ray Telescope Blank	Optical
D	100275	Support Strut	Optical
D	100288	Bench Support Panel	Optical
C	100302	Longerong	Optical
C	100322	Machine Drawing Invar Channel	Optical
C	100375	Filter Holder	Optical
D	100376	Prefilter Shutter	Optical
E	100377	Prefilter Housing	Optical
D	100386	Filter Microswitch Bracket	Optical
E	100388	Details Energy Absorber	Protection
E	100390-A	Mirror Support Barrel	Optical
E	100498	Mirror Mounting Ring	Optical
E	100553	Protection Device Details	Protection
E	100572-B	Front Support Plate	Optical
E	100594-A	Optical Bench Base Ring	Optical
E	100606-A	Middle Support Plate & Mirror Damper System	Optical
E	100656-A-1	70" Black Brant Payload Skin	Structure
D	100656-A-2	70" Black Brant Payload Skin	Structure
E	100661	Energy Absorber	Structure
D	100751	Telescope Mounting Illustration	Structure
E	100821	Fine Sun Sensor Adjustable Mount	Optical
D	100834	Orientation Drawing 27.050 cs	Structure
D	602-001	Filter Wheel Hardware (IV c Camera)	Camera
C	652-1100-3	Grazing Incidence Secondary Optic	GIRO
D	652-1101-3	Housing P Axis Translation	GIRO

Size	Drawing No.	Description	Subsystem
D	652-1102-2	Housing O Axis Translation	GIRO
C	652-1103-1	Housing Optical Axis Translation	GIRO
C	652-1104-2	Side Plate Optical Axis Housing	GIRO
C	652-1105-1	Yoke, Optic Mounting	GIRO
C	652-1106	Housing, Grazing Optic	GIRO
B	652-1107-2	Wedge, Linear Translation	GIRO
C	652-1108-2	End Cap, Yoke	GIRO
B	652-1109-1	Cover, Top Optical Axis Housing	GIRO
B	652-1110-3	Shaft Support w/ Spacer #1	GIRO
B	652-1111-1	Shaft Support w/ Spacer #2	GIRO
B	652-1112-1	Shaft Support w/ Spacer #3	GIRO
B	652-1113-1	Shaft Support w/ Spacer #4	GIRO
B	652-1114-1	Bar, Pivot	GIRO
B	652-1115-1	Wedge	GIRO
B	652-1116-1	Yoke	GIRO
B	652-1117-1	Plate, Spring Retainer	GIRO
A	652-1118-1	Screw, Special	GIRO
B	652-1119-1	Clamp	GIRO
C	652-1120-2	Shaft, P Axis	GIRO
B	652-1121-1	Holder, Linear Translation Wedge	GIRO
A	652-1122-1	Arm, Pivot	GIRO
E	652-1123-2	Ring, Tie In	Optical
B	652-1124-1	Rack, Gear	
B	652-1125-2	End Cap, Rack	
A	652-1126-1	Pusher, Rack	
C	652-1127-3	Support, Micrometer	GIRO
A	652-1128-1	Spacer, Micrometer Support	GIRO
A	652-1129-1	Retainer, Bearing	GIRO
B	652-1130-1	Ball Nut	GIRO
A	652-1131-1	Shaft, +O Axis Grazing Optic Housing	GIRO
A	652-1132-1	Shaft, -O Axis Grazing Optic Housing	GIRO
A	652-1133-1	Shaft, +P Axis Grazing Optic Housing	GIRO

Size	Drawing No.	Description	Subsystem
A	652-1134-1	Shaft, -P Axis Grazing Optic Housing	GIRO
B	652-1135-2	Support, Motor	GIRO
A	652-1136-1	Clamp, Wedge Linear Translation	GIRO
B	652-1137-1	Support, Worm	GIRO
E	652-1138-1	Grazing Incidence Relay Optics (GIRO) Assembly	GIRO
A	652-1139-1	Shaft, Worm	GIRO
A	652-1140-1	Bushing, Worm	GIRO
E	652-1141-4	Baseplate, GIRO	GIRO
A	652-1142	Clamp, Shaft -O, -P Axis	GIRO
A	652-1143-1	Spacer Linear Wedge	GIRO
A	652-1144-1	Pin, Spring	GIRO
A	652-1145-1	Cap, Micrometer	GIRO
B	652-1146-1	Clamp, P Axis Shaft	GIRO
B	652-1147-1	Container Stop Rack	GIRO
B	652-1148-1	Support Motor Mount	GIRO
A	652-1149-1	Rack, Stop	GIRO
A	652-1150-1	Pin, Grooved Spring	GIRO
E	652-1151	Optical Path, Ultra-High Resolution Imaging	Optical
B	652-1152-2	Shaft Support w/ Spacer #5 & #6	GIRO
A	652-1153-1	Bushing, Shaft Support Grazing Optic Housing	GIRO
C	652-1154-2	Launch Lock & Motor Drive Support Bracket	GIRO
B	652-1155-2	Launch Lock Rack Gear	GIRO
A	652-1156-1	Roller Launch Lock	GIRO
SK	652-1190-1	GIRO Mock-Up Piece	GIRO
E	652-1191-1	GIRO Mirror Layout	GIRO
E	652-1200	Primary Camera 45° Translation Mechanism	Camera

Size	Drawing No.	Description	Subsystem
E	652-1200-2	Primary Camera 45° Translation Mechanism	Camera
D	652-1201	Bearing Support Housing (RH) Primary Camera Translation Mechanism	Camera
D	652-1202	Bearing Support Housing	Camera
D	652-1203	Channel Bracket (LH)	Camera
C	652-1204-2	Shaft Support Block Primary Camera Translation Mechanism	Camera
C	652-1205-2	Motor Housing Block Primary Camera Translation Mechanism	Camera
D	652-1206	Angle Support Bracket	Camera
E	652-1207	Support Block (LH)	Camera
E	652-1208	Support Block (RH)	Camera
B	652-1209-5	Ball Screw Assembly Z Axis	Camera
B	652-1210-2	Ball Screw Assembly Y Axis	Camera
A	652-1214-2	3/8" Diameter Shaft Retainer	Camera
A	652-1216-4	Ball Screw Bearing Retainer	Camera
A	652-1217-2	Bushing	Camera
D	652-1220	Platform Sub-Assembly 45° Translation Mechanism	Camera
C	652-1221-1	Motor Support 45° Translation Mechanism	Camera
B	652-1222	Pulley Support 45° Translation Mechanism	Camera
A	652-1223	Shaft, Pulley-Idler Translation Mechanism	Camera
A	652-1224-1	Idler Pulley Translation Mechanism	Camera
B	652-1225	Bracket, Ball Nut Translation Mechanism	Camera
C	652-1226	Housing, Bearing Translation Mechanism	Camera
E	652-1227-1	Carriage, Camera Translation Mechanism	Camera

Size	Drawing No.	Description	Subsystem
B	652-1228	Idler Pulley Assembly Translation Mechanism	Camera
B	652-1229	Support, Idler 45° Translation Mechanism	Camera
B	652-1230	Support, Screw 45° Translation Mechanism	Camera
E	652-1300-2	Test Fixture, Optical Bench	Testing
D	652-1301	Weldment Angle Support	
D	652-1302	X-Axis Pivot Plate	
D	652-1303	Plat Y Axis	
A	652-1304-2	Angle Support Bracket, Test Fixture Optical Bench	Testing
D	652-1305	Optical Rail Baseplate Rework	
A	652-1306	Spacer .501 ID .750 OD x .25 thk	
A	652-1307	Adjustment Angle	
A	652-1308	"Y" Axis Control Pivot Plate	
D	652-1400	Optical Bench Attachment, End View	Optical
D	652-1401	Optical Bench Clearance Modification	Structure
E	652-2001-A	Assembly, CCD Camera Dewar Housing	CCD
D	652-2004	Connector Bracket, Housekeeping/Experiment Interface	Computer
D	652-2005	Housing, 4 Position Filter Wheel	CCD
D	652-2006	Housing, Rotating Shutter	CCD
B	652-2007	Motor Mount, Rotating Shutter Housing	CCD
B	652-2008	Bearing Plate, Geneva Wheel	CCD
B	652-2009	Bearing Plate, Geneva Driver	CCD
B	652-2010	Motor Mount, Optical Window Drive	CCD
B	652-2011	Drive Shaft, Optical Window Arm	CCD
B	652-2012	Filter Mount, Optical Window	CCD
B	652-2013	Latch Bracket, Dewar Housing	CCD
B	652-2014	Bearing Latch Bracket, Optical Window	CCD
B	652-2015	Latch Bracket, Dewar Housing	CCD

Size	Drawing No.	Description	Subsystem
	652-2016	Seal Plate, Optical Window	CCD
B	652-2017	Frame, Optical Window	CCD
B	652-2018	Bearing Latch Housing, Optical Window	CCD
SK	652-2019	PWB Rack, CCD & PCM Box	Structure
SK	652-2020	PWB Box, CCD & PCM	Structure
SK	652-2021	Top, CCD & PCM Box	Structure
SK	652-2022	Bottom, CCD & PCM Box	Structure
SK	652-2023	Card Support Rail, CCD & PCM Box	Structure
SK	652-2024	Connector Box, PCM	Structure
SK	652-2025	Connector Box, CCD	Structure
E	652-2032	Base Ring, Optical Bench	Structure
E	652-2033	Skin Section, Microcomputer	Structure
SK	652-2100	CCD Camera Orientation	CCD
SK	652-2101-2	Rotating Shutter	CCD
SK	652-2102	Shaft, Geneva Drive	CCD
SK	652-2103	Cover Plate, CCD Chip	CCD
SK	652-2104	Light Baffle, Electronic Shutter	CCD
SK	652-2105	Bracket, Hall Effect Sensor, Filter Wheel	CCD
SK	652-2106	Bracket, HAll Effect Sensor, Rotating Shutter	CCD
SK	652-2107	Cover Mount, CCD Chip	CCD
SK	652-2108	Anchor Stand-off, G10 Ring	CCD
SK	652-2109	Insulating Stand-off, Camera Head Electronics	CCD
SK	652-2110	Wire Shield, CCD Contacts	CCD
SK	652-2111	Magnet Holder, Filter Wheel	CCD
SK	652-2112	Connector Bracket, 15 Pin Cannon	CCD
SK	652-2113	Connector Bracket, 9 Pin Cannon	CCD
SK	652-2114	Stand-off Male/Female	CCD
SK	652-2115	Shaft, Filter Wheel	CCD
SK	652-2116	Anchor Stand-off, Cold Plate	CCD

Size	Drawing No.	Description	Subsystem
SK	652-2117	Holder, Filter Element	CCD
SK	652-2118	Filter Wheel	CCD
SK	652-2119	Cover, Filter Wheel Housing	CCD
SK	652-2120	Mask, Rotating Shutter	CCD
SK	652-2121	Rotating Shutter	CCD
SK	652-2122	Base Bracket, Inboard Longerong	CCD
SK	652-2123	Top Bracket, Inboard Longeron	CCD
SK	652-2124	Top Bracket, Outboard Longeron	CCD
SK	652-2125	Base Bracket, Outboard Longeron	CCD
SK	652-2126	Bracket, Winchester Connectors	CCD
SK	652-2127	Cold Plate, CCD Group	CCD
SK	652-2128	Support Gusset, Electronics Deck	CCD
SK	652-2129	Support Bracket, Rotating Shutter & Filter Wheel Housing	CCD
SK	652-2130	Contact Mount, CCD Chip	CCD
SK	652-2131	Outboard Longeron Dewar Support	CCD
SK	652-2132	Inboard Longeron Dewar Support	CCD
SK	652-2133	Link Arm, Optical Window	CCD
SK	652-2134	Base Cover, Dewar Housing	CCD
SK	652-2135-A	Additional Machining, Base Cover, Dewar Housing	CCD
SK	652-2136-A	Additional Machining, CCD Dewar Housing	CCD
SK	652-2137	Electronics Support Deck	CCD
SK	652-2138	CCD Camera Head Electronics Boxes	CCD
SK	652-2139	Adapter Plate, Calibration Chamber	CCD
SK	652-2140	Optical Window View w/ Armature	CCD
SK	652-2141	View, Rotating Shutter & Filter Wheel Housing	CCD
E	652-2200	Top Plate, Outer Ring Energy Absorber	Protection
E	652-2201	Base, Energy Absorber	Protection
SK	652-2202	Gravitational Acceleration Energy Displacement Unit Inner	Protection

Size	Drawing No.	Description	Subsystem
SK	652-2203-B	Base Plate, Shock Absorber	Protection
SK	652-2300	Frame, Prefilter	Optical
SK	652-2301	Base Plate, Camera Translation Drive	Camera
SK	652-2302	Focus Assist Plate, Mirror Support	Optical
SK	652-2303	HVSS Spring Placement	Structure
SK	652-2304	Separation Can, 36.058cs	Structure
SK	652-2305	Support Mast, Cable	Structure
SK	652-2306	Access Bracket, Housekeeping	Structure
SK	652-2307	Anchor Platform, Multidata Camera	Structure
SK	652-2308	Bracket, Left Camera Adjust	Camera
SK	652-2309	Carriage, Fixed, Multidata Camera	Camera
SK	652-2310	Bracket, Right Camera Adjust	Camera
SK	652-2311	Base Deck, Crush Pad	Protection
SK	652-2312	Top Deck, Crush Pad	Protection
SK	652-2313	Crush Pad	Protection
SK	652-2314	Payload Profile, 36.058cs, Controlled Payload Weight and CG	General
SK	652-2315	Payload Profile	General
	652-2316	Aft Can, Mirror Damper System	Protection
SK	652-2317	Camera Service Can Access Machining	Structure
	652-2318	Forward Can, Optical Bench	Structure
SK	652-2319	Aft Can, Optical Bench	Structure
SK	652-2320	Adapter Ring, Female/Female Tension Joint	Structure
SK	652-2321	Separation Retaining Plate	Structure
SK	652-2322	HVSS Detail	Structure
SK	652-2323	Interface Drawing, Separation Can	Structure
E	123XXXX	Inverted Payload SPARCS MASS/LISS Sensor Orientation	SPARCS
	652-2407	Additional Machining, Micro-computer/ Housekeeping Skin	Structure

Size	Drawing No.	Description	Subsystem
SK	652-2450	Preliminary Layout, Differential Assembly	Structure
SK	652-2451	Interface Drawing, HVSS & Crushable Section/Despin & Igniter Housing	Structure
	652-2452	Flight Configuration, High Resolution Imaging Payload	Structure
C-GEN-17155		HVSS Spring Assembly	Structure
D-005-12-E		Vacuum Shutter Control Circuit	Shutter
D-27-13946-C		Details, Shutter Plate	Shutter
D-27-13795-B		Shutter Extension Ring	Shutter
GD-34-1251		Ring, Manacle Type (Sheet 2)	Structure
GD-34-1251		Ring, Manacle Type (Sheet 3)	Structure
GD-34-1251		Ring, Manacle Type (Sheet 4)	Structure
D-GEN-15437		Igniter Housing, Black Brant	Structure
D-GEN-15871-A		HVSS/Shutter Assembly	Structure
D-GEN-16277		Shutter Assembly	Structure
D-GEN-16611		Longitudinal Deployment Gun Assembly	Structure
D-36-17242		Impact Energy Absorber Section	Structure
D-36-17404		FWD Can, Optical Bench Payload Skin	Structure
D-36-17405		Camera Service Can - Access Machining	Structure
D-36-17427		Female To Female Adapter	Structure
D-36-17428		AFT Can Optical Bench	Structure

SYSTEM DRAWINGS

D	652-0000	Giro Solar Rocket - System Block Diagram	GIRO
D	652-0001	Giro Solar Rocket - Telemetry Links	GIRO
D	652-0002	Giro Solar Rocket - Power Profile	GIRO

Size	Drawing No.	Description	Subsystem
		GIRO COMPUTER BOARDS	
D	652-3100	CPU - Logic Diagram	CPU
D	652-3101	Printed Wiring Master	CPU
D	652-3102	Printed Wiring Assembly	CPU
D	652-3103	Printed Wiring Board	CPU
D	652-3110	Memory & I/O #1 - Logic Diagram	
D	652-3111	Printed Wiring Layout - Memory & I/O #1	
D	652-3113	Printed Wiring Board - Memory & I/O #1	
D	652-3120	Monitor Drivers, Isolators and Timer Logic Diagram	
D	652-3121	Printed Wiring Master - Monitor Drivers, Isolators and Timer	
D	652-3123	Printed Wiring Board - Monitor Drivers, Isolators and Clock	
D	652-3130	Memory, Power Fail, Test Buffers - Logic Diagram	
D	652-3131	Printed Wiring Master - Memory, Power Fail, Test Buffers	
D	652-3133	Printed Wiring Board - Memory, Power Fail, Test Buffers	
D	652-3140-1	Memory & I/O #2-1 - Logic Diagram	
D	652-3140-2	Memory & I/O #2-2 - Logic Diagram	
D	652-3141	Printed Wiring Master	
D	652-3143	Printed Wiring Board	
D	652-3150	Output Signal Conditioning - Logic Diagram	
D	652-3151	Printed Wiring Master	
D	652-3152	Assembly	
D	652-3153	Printed Wiring Board	
D	652-3160-1	Input Conditioning & Buffers #1 - Logic Diagram	

Size	Drawing No.	Description	Subsystem
D	652-3160-2	Input Conditioning & Buffers #2 - Logic Diagram	
D	652-3161	Printed Wiring Master	
	652-3162	Assembly	
D	652-3163	Printed Wiring Board	
D	652-3170	Monitors - Logic Diagram	
D	652-3171	Printed Wiring Master	
	652-3172	Assembly	
D	652-3173	Printed Wiring Board	
D	652-3180	Bus Buffer & Buffers - Logic Diagram	
D	652-3181	Printed Wiring Master	
	652-3182	Assembly	
	652-3183	Printed Wiring Board	
D	652-3190	Power Board - Logic Diagram	

CCD CAMERA

	652-2511	CCD Camera - Edge Connector Wiring	CCD
A	652-4000	PL, PW Assy, Memory Board "B" - 27.074 CCD Camera	CCD
C	652-4100	Diagram, Memory Board "B" - 27.074 CCD Camera	CCD
D	652-4300	Master Patt, Memory Board "B" - 27.074 CCD Camera	CCD
D	652-4200	PW Board, Memory Board "B" - 27.074 CCD Camera	CCD
A	652-4001	PL, PW Assy, Raster Limit Board "D" - 27.074 CCD Camera	CCD
C	652-4101	Diagram, Raster Limit Board "D" - 27.074 CCD Camera	CCD
D	652-4301	Master Patt, Raster Limit Board "D" - 27.074 CCD Camera	CCD

Size	Drawing No.	Description	Subsystem
D	652-4201	PW Board, Raster Limit Board "D" - 27.074 CCD Camera	CCD
A	652-4002	PL, PW Assy, Camera Micro-Controller Board "J" - 27.074 CCD Camera	CCD
C	652-4102	Diagram, Camera Micro-Controller Board "J" - 27.074 CCD Camera	CCD
D	652-4302	Master Patt, Camera Micro-Controller Board "J" - 27.074 CCD Camera	CCD
D	652-4202	PW Board, Camera Micro-Controller Board "J" - 27.074 CCD Camera	CCD
A	652-4003	PL, PW Assy, ACD Board "I" - 27.074 CCD Camera	CCD
C	652-4103	Diagram, ACD Board "I" - 27.074 CCD Camera	CCD
D	652-4303	Master Patt, ACD Board "I" - 27.074 CCD Camera	CCD
D	652-4203	PW Board, ACD Board "I" - 27.074 CCD Camera	CCD
A	652-4004	PL, PW Assy, Correlated Double Sample/Hold, Board "H" - 27.074 CCD Camera	CCD
D	652-4104	Diagram, Correlated Double Sample/Hold 27.074 CCD Camera	CCD
D	652-4304	Master Patt, Correlated Double Sample/ Hold - 27.074 CCD Camera	CCD
D	652-4204	PW Board, Correlated Double Sample/Hold 27.074 CCD Camera	CCD
A	652-4005	PL, PW Assy, Clock Control Board "A" - 27.074 CCD Camera	CCD
C	652-4105	Diagram, Clock Control Board "A" - 20.074 CCD Camera	CCD
D	652-4305	Master Patt, Clock Control Board "A" -	CCD

Size	Drawing No.	Description	Subsystem
		20.074 CCD Camera	
D	652-4205	PW Board, Clock Control Board "A" - 20.074 CCD Camera	CCD
A	652-4006	PL, PW Board, Telemetry Micro-Controller Board	CCD
D	652-4106	Diagram Telemetry Micro-Controller Board "K" - 27.074 CCD Camera	CCD
D	652-4306	Master Patt, Telemetry Micro-Controller Board	CCD
D	652-4206	PW Board, Telemetry Micro-Controller Board	CCD
A	652-4007	PL, PW Assy, CCD Head Electronics Board	CCD
D	652-4107	Diagram, CCD Head Electronics Board - 27.074 CCD Camera	CCD
D	652-4307	Master Patt, CCD Head Electronics Board	CCD
D	652-4207	PW Board, CCD Head Electronics Board	CCD
A	652-4008	PL, PW Assy, Data Interface Board	CCD
D	652-4108	Diagram, Data Interface Board - 27.074 CCD Camera	CCD
D	652-4308	Master Patt, Data Interface Board	CCD
D	652-4208	PW Board, Data Interface Board	CCD
A	652-4009	PL, PW Assy, Temperature Monitor & Controller Board	CCD
D	652-4109	Diagram, Temperature Monitor & Controller Board	CCD
D	652-4309	Master Patt, Temperature Monitor & Controller Board	CCD
D	652-4209	PW Board, Temperature Monitor & Controller Board	CCD

Size	Drawing No.	Description	Subsystem
		TEST SET BOARDS	
C	652-5102	Schematic, Camera Micro-Controller, CCD Camera Test Set	CCD
D	652-5106	Schematic, PCM Telemetry Micro-Controller CCD Camera Test Set	CCD
D	652-5108	Schematic, Data Interface CCD Camera Test Set	CCD
D	652-5111	CCD Camera Test Set Ver. 2, Edge Conn Wiring	CCD